Energy & Buildings 256 (2022) 111751

Contents lists available at ScienceDirect

Energy & Buildings

journal homepage: www.elsevier.com/locate/enb

Performance of lightweight and heavyweight building walls with naturally ventilated passive and active facades

Mohammad Rahiminejad [a,*], Alexandre Louis Marie Pâris [a], Hua Ge [b], Dolaana Khovalyg [a]

[a] Thermal Engineering for the Built Environment Laboratory (TEBEL), Ecole Polytechnique Fédérale de Lausanne (EPFL), Lausanne, Switzerland
[b] Department of Building, Civil and Environmental Engineering, Concordia University, Montreal, QC, Canada

ARTICLE INFO

Article history:
Received 21 August 2021
Revised 21 November 2021
Accepted 29 November 2021
Available online 7 December 2021

Keywords:
Ventilated air-space
Thermal inertia
Passive cladding
BIPV façade
Numerical model

ABSTRACT

Well-designed ventilated air-spaces behind external claddings in the building envelope can potentially reduce thermal energy flow in the entire wall structure. In this study, the impact of the dynamic thermo-hydraulic behavior of the flow in the naturally ventilated cavity on the performance of lightweight and heavyweight wall assemblies with traditional passive and active (i.e., BIPV) facades is investigated. A numerical transient 2-D model validated against experimental measurements is employed to perform the analysis using actual weather data and building practices in Europe, particularly in Switzerland. The results reveal that the change in the external cladding type from the passive fiber cement to the active PV façade can increase the time lag of the wall structure up to 2 h in summer and decrease it up to 1 h in winter. The maximum difference between the amplitudes of the heat flux through the interior surface for a wall assembly with the lightweight wall core is 1.5 times higher compared to a heavyweight wall core. The results show that enlarging the cavity thickness behind external claddings from 45 mm to 110 mm can increase the heat flow through the cavity up to 1.5 times. It is also shown that reflective insulation on the cavity surface adjacent to the wall core could increase the cladding surface temperature by more than 30% compared to the case without reflective insulation. This research shows that replacing the passive cladding with an active façade could affect the performance of the entire wall assembly, which highlights the importance of analyzing the active ventilated wall structures to transition towards modern building skins.

1. Introduction

Photovoltaic (PV) applications in buildings have been attracting interest in recent years and becoming the backbone of the zero energy building European target [38]. Due to the lack of available capacity of energy production in a dense urban area, Building Integrated Photovoltaic (BIPV) technology has been promising to play an essential role in the on-site production of electricity. In particular, the BIPV façade concept is based on the idea of using PV modules as an external cladding that not only meets the construction requirements but also produces electricity [61] .

Similar to the traditional cladded wall assemblies, where a ventilated cavity could separate the external cladding from the wall core, the presence of sub-frames in the BIPV systems creates a ventilated air-space behind the PV panels. The primary purpose of using ventilated air gaps in the traditional wall structures is to control excessive moisture accumulated in the absorbent materials [68]. Ventilation behind the cladding can also enhance the thermal performance of the building envelope [1]. In the modern BIPV facade systems, the presence of the ventilated air-space could be even more beneficial. The airflow through the ventilated cavity can remove the dissipated heat from the back of the module, decrease the temperature of its surface, and eventually increase the electrical efficiency of the PV panels [36]. Therefore, the ventilated air gap behind BIPV facades can contribute both to the electrical efficiency of PV modules and the thermal efficiency of the wall assembly.

Generally, the thermo-hydrodynamic performance of the ventilated air gap is a function of multiple parameters. Different hygrothermal aspects of the ventilated cavity incorporated in the exterior surface of the traditional wall assemblies have been investigated in the literature [25,43,42,39,74,14,46,71,11,20,23,66,48,52,19,26,51]. The air change rate in the air-space has been shown to have a considerable impact on the amount of heat flux passing through the wall structure [54]. A comprehensive literature review on the factors affecting the airflow rate in the ventilated air-spaces

* Corresponding author at: EPFL Antenna Fribourg Passage du Cardinal 13b, CH-1700 Fribourg, Switzerland.
E-mail address: mohammad.rahiminejad@epfl.ch (M. Rahiminejad).

https://doi.org/10.1016/j.enbuild.2021.111751
0378-7788/

Nomenclature

Symbol	Definition [Unit]
A	Cross-sectional area of opening [m^2]
c_p	Heat capacity [J/kg K]
c	Specific heat capacity [J/K]
$_{CD}$	Wind pressure coefficient [-]
D	Thickness of the material [m]
$_Dh$	Hydraulic diameter [m]
F	Decrement factor [-]
fr	Friction factor [-]
F	View factor [-]
g	Acceleration due to gravity [m/s^2]
G	Solar radiation [W/m^2]
h	Heat transfer coefficient [W/m^2 K]
k	Thermal conductivity [W/m K]
K	Minor loss coefficient
L	Height [m]
m	Vertical position
M	Mass flow rate [kg/s]
q	Heat flux [W/m^2]
R	Thermal resistance [m K/W]
ΔR	Extra infrared radiation factor [W/m^2]
t	Time [s]
T	Temperature [K]
V	Velocity [m/s]
w	Cavity width [m]
Re	Reynolds number [-]
Gr	Grashof number [-]
Ra	Rayleigh number [-]
Nu	Nusselt number [-]
Ri	Richardson number [-]
Pr	Prandtl number [-]
Δx	Length of the horizontal step [m]
Δy	Length of the vertical step [m]
Δt	Time step period [s]
ε	Surface emissivity [-]
α	Absorptivity [-]
ϕ	Time lag [h]
β	Thermal expansion coefficient [1/K]
τ	Transmittance [-]
η_e	Electrical efficiency [-]
γ	Temperature coefficient of electrical power [W/K]
θ	Angle of inclination with the horizontal (°)
σ	Stefan-Boltzmann constant [W/m^2K^4]
ρ	Density [kg/m^3]
μ	Dynamic viscosity [kg/m s]

Subscripts

Symbol	Definition
air	Air
Amb	Ambient
c	convection
Cav	Cavity
cl	Cladding
EVA	EVA layer
ext	Exterior
for	Forced convection
For L	Forced convection and laminar flow
For T	Forced convection and turbulent flow
FP	Fiber plaster
G	Glass layer
I	Timestep
Ind	Indoor
int	Interior
ins	Insulation layer
jc	Jute coating
L	Left
m	Vertical position
M	Last vertical position of the height
Mix	Mixed convection
n	Horizontal position
N	Last horizontal position of a material layer
Nat	Natural convection
natL	Natural convection and laminar flow
natT	Natural convection and turbulent flow
PV	PV layer
r	Radiation
R	Right
Ref	Reference
Sky	Sky
Surr	Surrounding
T	Tedlar back sheet

behind various types of traditional opaque external claddings is performed by Rahiminejad and Khovalyg [55]. The ventilation rates in the cavities behind different types of façades reported in the literature are collected, and the forces that drive the airflow inside the cavity are described. In the other studies by Rahiminejad and Khovalyg [56–58], the plausible definitions and recommendations for measuring the thermal resistance of the ventilated air gap behind vertical external claddings are provided, and it is shown that the thermal resistance of a ventilated air-space can vary significantly depending on various thermo-physical properties of the entire wall assembly. The dynamic thermal performance of the building envelope integrating BIPV façade has also been thoroughly analyzed in the previous studies [77,15,29,18,5]. An experimental study conducted by Chiu et al. [15] demonstrated an improvement in the overall heat transmittance of the naturally ventilated BIPV wall compared to the non-ventilated assembly. Dehra [18] presented an investigation on energy performance assessment of a ventilated photovoltaic solar wall using either a buoyancy-induced or fan-assisted ventilation system in the air cavity. The energy analysis performed for the two systems demonstrated that the operation of the fan-assisted ventilation system achieved better performance.

In addition to the presence of the ventilated air-space and the type of the external cladding, the thermal mass of the layers used in the wall core has a considerable influence on the thermal performance of the building envelope. The amplitude of energy flow through a wall assembly could be reduced by employing the absorption and retention ability of thermal mass building components, thus, resulting in moderate internal surface temperature fluctuations. The time needed for a heatwave to propagate from the outer surface to the inner surface, i.e., "time lag", and the decreasing ratio of its amplitude during this process, i.e., "decrement factor", are the two main factors that describe the transient response of the building envelope. The effect of the thermal inertia of the materials used in the wall structure on the aforementioned factors has been widely investigated in the previous studies for the wall assemblies with traditional external claddings [7,73,8,10,28,41,59]. Aste et al. [10] investigated the influence of thermal inertia of the external walls on the energy performance of residential buildings in Italy. It was shown that the difference

between the heating demand in low inertia and high inertia wall could be 10%. This value reached 20% in the case of cooling demand. Guillén et al. [28] used a numerical model to determine the thermal behavior of two ventilated facades with different thermal mass values. It is concluded that the increase in the use of thermal insulation in the wall affects the associated time lag.

Despite many studies available for the wall structures with traditional claddings, a few studies evaluated the impact of the thermal inertia of the wall assembly on the transient response of the building envelope constituted of BIPV systems. Wang et al. [76] developed a one-dimensional transient heat-transfer model for integrating PV systems into the roofs of a building. It is shown that the BIPV roof with the ventilated cavity has the optimum performance in summer conditions. The authors stated that the PV roof with a ventilated air-space has higher time-lag and smaller decrement factor compared to the system with an enclosed air-space. Meyer et al. [47] measured the thermal efficiency of a BIPV roof system. The results in winter showed a time lag of 2 h and a decrement factor of 0.67, while the time lag was increased to 3 h and the decrement factor decreased to 0.56 during the summer. Heim and Wieprzkowicz [31] proposed a novel composite modified by phase change material to attenuate the fluctuations of the external surface temperature of a building prototype in a period of significant heat gains. A ventilated air-space separates the wall core covered with the BIPV panels. Although the results showed that the proposed composite material could have higher heat storage potential compared to the traditional high-density mineral wool, the influence of the BIPV façade on the observations has not been adequately analyzed, and the main focus of this research was on the composite material.

The transition from traditional claddings towards BIPV façades with different thermo-physical properties has made the necessity of analyzing the thermal performance of the modern upcoming wall structures undeniable. Although different aspects of this transition have been investigated in the previous studies, the abovementioned literature review shows that there is still a lack of research addressing the impact of thermal inertia on the thermal performance, electrical efficiency, and transient responses of a ventilated wall structure with modern BIPV façades. Since the thermo-hydrodynamic behavior of the air in the ventilated air-space behind the PV modules could potentially contribute to the thermal performance of the entire wall assembly, the present work aims to employ a transient numerical model and compare the thermal performance of a lightweight and heavyweight building wall with the passive (traditional) and active (BIPV) external claddings. The further objectives of this study are to investigate the effect of the seasonal variation, the thickness of the ventilated air gap, and the emissivity of cavity surface on the thermal and electrical efficiency of the naturally ventilated BIPV wall assemblies. The size of the "ventilated air-space" considered in this paper is limited to 150 mm, and wider air gaps typical for Double Skin Facades are not considered.

2. Methodology

2.1. Case study scenarios

The present study aims to compare passive and active cladding systems mounted on the wall core that is made up of either a light or heavy mass load-bearing wall, as shown in Fig. 1. The passive facade is a fiber cement board, and it is replaced by a typical polycrystalline photovoltaic module in the active façade. The PV module consists of multiple layers, including tempered glass, photovoltaic cells encapsulated between ethyl vinyl acetate (EVA) layers, and a polymer back sheet. The height of the wall is taken as 1.64 m, corresponding to the height of a standard polycrystalline PV module [3]. An overview of materials used in the EU and Swiss housing stock shows that the reinforced concrete wall is among the most common layers in the wall assembly that are contemporary being used in the region [50,63]. However, the use of wood has been increased over the past decades due to its sustainability and environmental qualities [63]. Therefore, these two materials are selected as the load-bearing layer in the wall core to represent a heavyweight and lightweight wall core, respectively.

The typical thicknesses considered for the concrete block and the timber hardwood are 150 mm and 100 mm suggested by Swisspor [70]. The inner side of the load-bearing wall is protected by a 10 mm fiber plasterboardSwisspor [70]. To insulate the wall core, a layer of expanded polystyrene placed on the outer side of the load-bearing wall is used. The thickness of the insulation layer varies depending on the overall transmittance value of the façade obtained using the ISO 6946 [33] recommendations. The insulation thickness has been sized to have a similar U-value for both lightweight and heavyweight wall assemblies that is equal to 0.16 W/($m^2 \cdot K$). The U-value complies with the Swiss building code SIA 380/1, which requires 0.17 W/($m^2 \cdot K$) for the opaque façades of new buildings. The thickness of the insulation is determined to be equal to 170 mm and 160 mm for the heavyweight and lightweight wall structures. The values are determined by fixing the thickness of the layers of the wall assembly (excluding insulation) and using the thermophysical properties of the materials listed in Table 1 [33]. The thickness of the air gap behind the external cladding is either 45 mm or 110 mm. The selected two values represent the presence of both thin and thick cavities behind the traditional and BIPV façades. The former is recommended for a passive ventilated façade [78], and the latter is the optimal width to minimize the PV overheating [24]. The presence of reflective insulation attached to the cavity wall adjacent to the wall core is also modeled to compare the impact of the low emissivity and high emissivity cavity surface on the thermal performance of the wall assembly.

The effect of seasonal variation is investigated for the *typical* and *extreme* days in summer and winter of 2019 using the weather data of Lausanne [44], Switzerland, which represents a temperate oceanic climate (i.e., Cfb) specified by Köppen [37]. The description of the simulated cases is provided in Table 2. In total, 32 scenarios are simulated on typical days by considering all combinations of various parameters. Additional 8 cases on extreme days are also simulated for selected parameters. Different cases simulated in this study are abbreviated in the hereafter text by assigning the letters provided in parenthesis in Table 2 to represent the condition of the case study. For instance, *LP-TS45* ε indicates the case study of a Lightweight (L) wall core with Passive (P) cladding in a Typical (T) Summer (S) day with 45 mm (45) air gap behind the façade and the presence of reflective insulation (ε) on the cavity surface adjacent to the wall core.

2.2. Numerical model

2.2.1. System discretization and assumptions

The multi-layer ventilated wall assembly is numerically modeled in MATLAB® employing a finite-difference method. An illustration of the parameters used in the model of the active façade is shown in Fig. 2. The numerical procedure used for determining the unknown parameters in the active ventilated wall assembly is elaborated in this section. The same method is used in the case of the passive façade by replacing the BIPV façade with fiber cement. The input parameters include the geometrical and thermal properties of each layer in the system, as well as the indoor and outdoor conditions. Therefore, the system is divided into control volumes, and a two-dimensional nodal network with 5 nodes

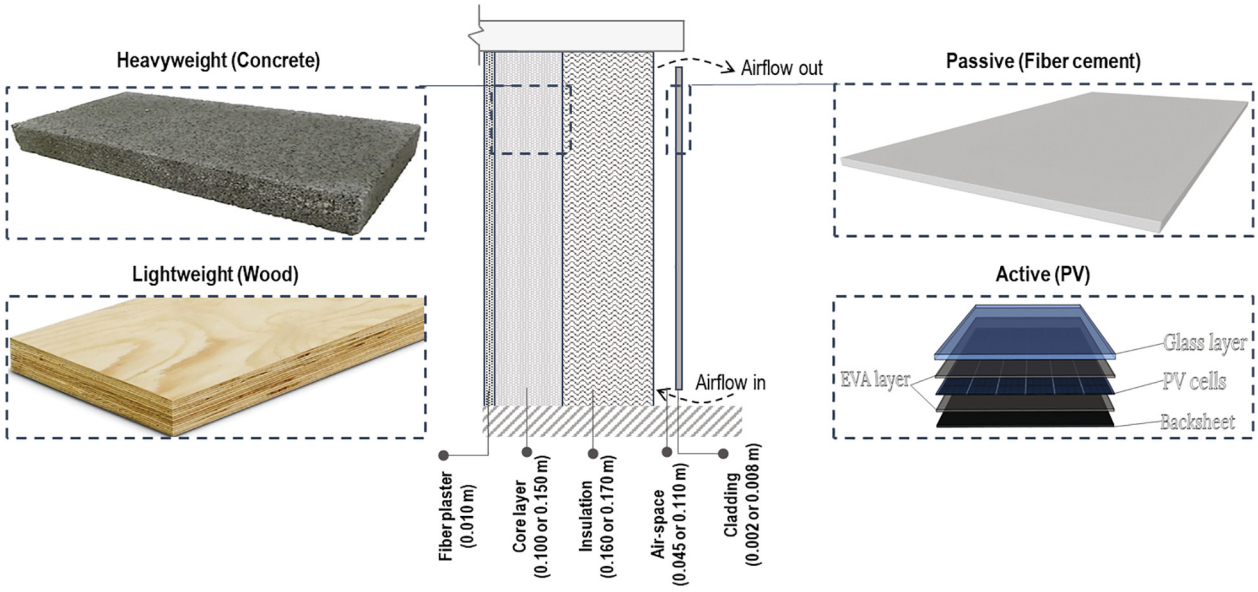

Fig. 1. Different ventilated wall assemblies simulated (refer to Table 1 for more information on the thermo-physical properties of each layer).

Table 1
Thermo-physical properties of the wall layers modeled [5,35,72].

Parameter	d	k	ρ	c_p	ε	α	τ
Unit	m	W/(m · K)	kg/m^3	J/kg·K	[-]	[-]	[-]
Active facade							
Tempered glass	0.0036	1.8	3000	500	0.88	0.10	0.90
EVA film	0.0004	0.35	960	2090	–	–	–
PV cells	0.0004	148	2330	700	–	0.90	–
Back sheet	0.0004	0.13	1450	1650	0.87	0.90	–
Passive facade							
Fiber cement	0.008	0.58	1900	1000	0.90	0.70	–
Heavyweight wall core							
Reflective insulation	0.0002	235	2700	890	0.05	0.04	–
Insulation	0.170	0.03	25	1380	0.90	–	–
Concrete	0.150	0.5	1400	1000	–	–	–
Fiber plaster	0.010	0.18	837	800	0.90	–	–
Lightweight wall core							
Reflective insulation	0.0002	235	2700	890	0.05	0.04	–
Insulation	0.160	0.03	25	1380	0.90	–	–
Wood	0.100	0.14	400	1255	–	–	–
Fiber plaster	0.010	0.18	837	800	0.90	–	–
Air cavity	0.045, 0.110	varies*	varies	varies	–	–	–

* The air properties vary as a function of the air temperature.

Table 2
Different scenarios simulated (abbreviations are shown in parentheses).

Day of interest	Parameter									
	Thermal mass		Cladding		Season		Cavity thickness (mm)		Reflective insulation	
	Lightweight (L)	Heavyweight (H)	Passive (P)	Active (A)	Summer (S)	Winter (W)	45 (45)	110 (110)	Absence (none)	Presence (ε)
Typical	✓	✓	✓	✓	✓	✓	✓	✓	✓	✓
Extreme	✓	✓	✓	✓	✓	✓	✓	✗	✓	✗

along with the height (m = 5 in Fig. 2) and 3 nodes through the depth of the geometry (n = 3 in Fig. 2) is created. The simulations for each day of interest are performed using 32 h of weather data that includes 8 h prior to the chosen day (16:00–00:00) to ensure the stability of the model; results for 8 prior hours are not considered. Some assumptions are made in the calculation process, including the fully developed flow across the width of the air cavity, no temperature drop at the interfaces, constant properties of the materials across the entire layer, and overtime, no infiltration through the photovoltaic wall section and the building materials, and negligible effects of the studs, junctions, and connections.

2.2.2. Governing equations

The temperature distribution T in the entire wall structure in two directions (x and y) is governed by Fourier's law of heat conduction in Cartesian coordinates (equation (1)) aided with Taylor's

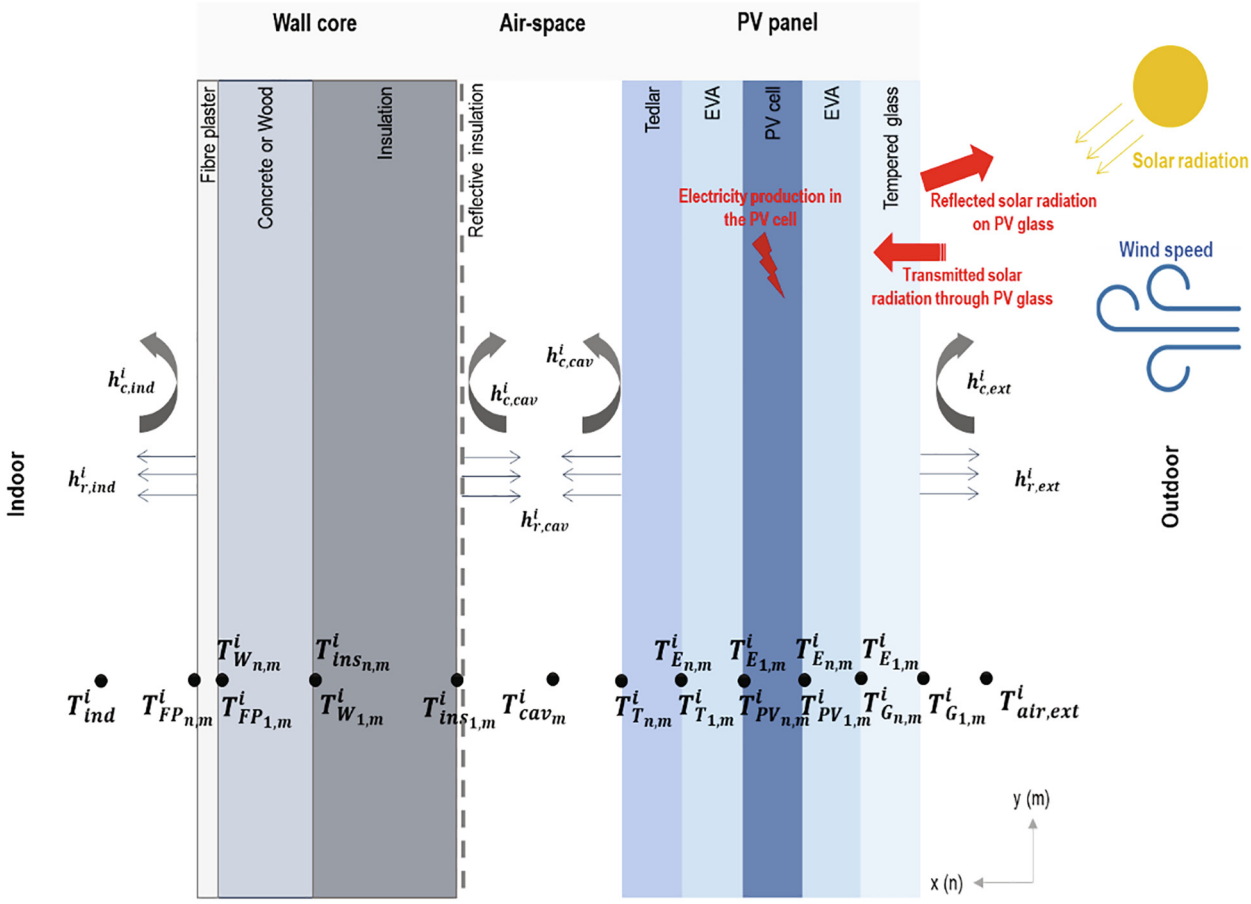

Fig. 2. Parameters used in the thermal analysis at a fixed time step (the dimensions are not scaled, the temperatures on the middle section of each layer are not shown, and indices are only shown on the edges).

series expansion, where $\dot{q}$ is the net heat flux in W/m^3 refers to the generated heat in the PV cell.

$$\frac{c_p\rho}{k}\frac{dT}{dt} = \frac{\partial^2 T}{\partial x^2} + \frac{\partial^2 T}{\partial y^2} + \frac{\dot{q}}{k} \tag{1}$$

where k is conductivity in W/m · K, ρ is density in kg/m^3, and c_p is the specific heat capacity in J/K.

The explicit finite difference scheme is employed to calculate the temperature variation of each node of the discretized network. The temperature of a particular node at time $t + 1$ is obtained based on the temperature of the same node and adjacent nodes at the previous time step t. After rearranging with the first and the second derivatives at the location (n, m) in the layer and time step i, equation (1) becomes:

$$T^{i+1}_{n,m} = T^{i}_{n,m} + \left(\frac{k\Delta t}{c_p\rho}\right)\left(\frac{1}{\Delta x^2}\left(T^{i}_{n-1,m} - 2T^{i}_{n,m} + T^{i}_{n+1,m}\right) + \frac{1}{\Delta y^2}\left(T^{i}_{n,m-1} - 2T^{i}_{n,m} + T^{i}_{n,m+1}\right) + \frac{1}{k\Delta x}q^{i}_{m}\right) \tag{2}$$

The net heat flux ${q_{n,m}}^i$ in the previous equations can be expressed as a function of different parameters in the particular layer, as detailed in the following sections.

For the tempered glass

The tempered glass is in direct contact with the outdoor environment. The net heat flow through the external surface q includes the absorbed solar irradiance combined with the transmittance and reflection between the tempered glass and PV cells, the radiative heat transfers with the sky, the surrounding and the ground, and the air-glass convective heat transfer. The net heat flux with the outdoor environment can be expressed as:

$$\begin{aligned} q^i_m = {} & \alpha_{O,G}G^i + h^i_{r,ext,Skym}\left(T^i_{Sky} - T^i_{G1,m}\right) \\ & + \sigma h^i_{r,ext,Ground}\left(T^i_{Ground} - T^i_{G1,m}\right) + h^i_{r,ext,Surrm}\left(T^i_{Surr} - T^i_{G1,m}\right) \\ & + h^i_{c,ext}\left(T^i_{air,ext} - T^i_{G1,m}\right) \end{aligned} \tag{3}$$

where G is solar radiation in W/m^2, α is solar absorptivity, σ is the Stefan-Boltzmann constant in W/m^2 · K^4, and h is the radiative heat transfer correlation in W/m^2 · K.

According to Holman [32], the radiative heat transfer coefficient between the glass and the sky, between the glass and the ground, and between the glass and the surrounding should be expressed as:

$$h^i_{r,ext,Skym} = \sigma\varepsilon_G F_{G-SKY}\left(T^{i2}_{Sky} + T^{i2}_{G1,m}\right)\left(T^i_{Sky} + T^i_{G1,m}\right) \tag{4}$$

$$h^i_{r,ext,Groundm} = \sigma\varepsilon_G F_{G-GROUND}\left(T^{i2}_{Ground} + T^{i2}_{G1,m}\right)\left(T^i_{Ground} + T^i_{G1,m}\right) \tag{5}$$

$$h^i_{r,ext,Surrm} = \sigma\varepsilon_G F_{G-SURR}\left(T^{i2}_{Surr} + T^{i2}_{G1,m}\right)\left(T^i_{Surr} + T^i_{G1,m}\right) \tag{6}$$

where ε is emissivity and F is the view factor.

The glass-to-sky, glass-to-surrounding, and glass-to-ground view factors are calculated as a function of the PV panel angle equal to 90° in the case of BIPV façade:

$$F_{G-SKY} = \frac{1+cos(\theta)}{2} cos\left(\frac{\theta}{2}\right) = \frac{\sqrt{2}}{4} \tag{7}$$

$$F_{G-GROUND} = \frac{1-cos(\theta)}{2} = \frac{1}{2} \tag{8}$$

$$F_{G-SURR} = 1 - F_{G-SKY} - F_{G-GROUND} = \frac{2-\sqrt{2}}{4} \tag{9}$$

The ground and the surrounding temperature are assumed equal to the ambient air temperature, while the sky temperature is approximated by Swinbank [69] as a function of ambient air temperature.

$$T^i_{Sky} = 0.0552\left(T^i_{air,ext}\right)^{1.5} \tag{10}$$

The external convective heat transfer coefficient is calculated based on the Nusselt number correlation by using the length of the wall L in m and the properties of air at the mean air temperature:

$$h^i_{c,ext} = \frac{Nu^i k^i_{air,ext}}{L} \tag{11}$$

The external convective heat transfer coefficient varies depending on the forced, natural, or mixed convection regime. The Reynolds number Re and the Grashof number Gr are used to determine the type of convection i.e., Gr^i/Re^{i^2}. In natural convection regime due to air buoyancy, i.e., $Gr^i/Re^{i^2} \gg 1$, Churchill and Chu [17] proposed the following correlation for the Nusselt number is used:

$$Nu^i_{ext-nat} = 0.68 + 0.67Ra^{i^{1/4}}\left[1+\left(\frac{0.492}{Pr^i}\right)^{9/16}\right]^{-4/9} \tag{12}$$

In a forced convection regime where the wind effect is dominant, i.e., $Gr^i/Re^{i^2} \ll 1$, the formulation given by Nusselt and Jürges [49] is used by considering the wind speed V in m/s.

$$Nu^i_{ext-for} = \frac{\left(5.8+3.94V^i_{air,ext}\right)L}{k^i_{air,ext}} \tag{13}$$

In the case of mixed convection regime, i.e., $Gr^i/Re^{i^2} \approx 1$, the equation recommended by Incropera [34] is used to combine the two previous correlations:

$$Nu^i_{ext-mix} = \sqrt[3]{Nu^{i^3}_{ext-nat} + Nu^{i^3}_{ext-for}} \tag{14}$$

Within the PV layer

At the PV layer surface, the absorbed solar irradiance by the PV layer and the conductive heat flow between the first and second EVA layers are considered.

$$T^{i+1}_{PVn,m} = T^{i+1}_{PVn,m} + \left(\frac{k_{PV}\Delta t}{c_{pPV}\rho_{PV}}\right)\left[\frac{1}{\Delta x^2}\left(T^i_{PVn-1,m} - 2T^i_{PVn,m} + T^i_{PVn+1,m}\right) + \frac{1}{\Delta y^2}\left(T^i_{PVn,m-1} - 2T^i_{PVn,m} + T^i_{PVn,m+1}\right) + \frac{1}{k_{PV}\ \Delta x}\left(\alpha_{PV}\ \tau_G\beta_{PV}G^i\left(1-\ \eta^i_{en,m}\right)\right)\right] \tag{15}$$

where τ is the transmittance of the PV and β is the thermal expansion coefficient in 1/K.

The electrical efficiency η depends linearly on the operating temperature and decreases when the PV cell temperature is higher than the reference temperature $T_{PV,ref}$ given by the manufacturer. The electrical efficiency of the PV cell nodes $\eta^i_{en,m}$ can be calculated as below:

$$\eta^i_{en,m} = \eta_{e,ref}\ + \gamma\left(T^i_{PVn,m} - T_{PV,ref}\right) \tag{16}$$

where the temperature coefficient of electrical power in W/K is $\gamma = -0.0004, \eta_{e,ref}$= 0.12, and $T_{PV,ref}$ is considered equal to 298 K [5] .

Tedlar surface

At the Tedlar surface adjacent to the air gap, the convective heat transfers with the air gap and the radiative heat transfer with the insulation layer are considered:

$$q^i_m = h^i_{c,cav,Tm}\left(T^i_{TN,m} - T^i_{cavm}\right) + h^i_{r,cavm}\left(T^i_{TN,m} - T^i_{Ins1,m}\right) \tag{17}$$

The radiative heat transfer coefficient between the back-sheet surface and the top surface of the insulation can be expressed as follows:

$$h^i_{r,cavm} = \frac{\sigma\left(T^{i2}_{TN,m} + T^{i2}_{Ins1,m}\right)\left(T^i_{TN,m} + T^i_{Ins1,m}\right)}{1/\varepsilon_T + 1/\varepsilon_{Ins} - 1} \tag{18}$$

Within the air gap

The convective heat transfer coefficient within the air channel is a result of energy transfer between the moving fluid and the solid surfaces, and it depends on the convection mode, as well as the flow regime in the channel. As the convective heat transfer coefficient relies on the air gap surface temperature, two coefficients $h_{c,cav,T_m}{}^i$ and $h_{c,cav,Ins_m}{}^i$ are calculated for each surface using similar correlations. The convective heat transfer coefficient is a function of the Nusselt number correlation by using the properties of air at the air gap temperature, where $D_h$is a hydraulic diameter in m.

$$h_{c,cav_m}{}^i = \frac{Nu^i_m k_{cav_m}{}^i}{D_h} \tag{19}$$

In natural convection regime caused by buoyancy forces, i.e., $Gr^i/Re^{i^2} \gg 1$, the average natural convection heat transfer coefficient between a flat plate is given by Incropera [34] as follow:

For a laminar regime ($Ra^i_m < 10^9$)

$$Nu_{cav-natL^i_m} = \frac{0.68 + 0.67Ra^{i\ 1/4}_m}{\left[1+\left(\frac{0.492}{Pr^i_m}\right)^{9/16}\right]^{4/9}} \tag{20}$$

For a turbulent flow ($Ra^i_m > 10^9$)

$$Nu_{cav-natT^i_m} = \left[0.825 + \frac{0.387Ra^{i\ 1/6}_m}{\left[1+\left(\frac{0.492}{Pr^i_m}\right)^{9/16}\right]^{8/27}}\right]^2 \tag{21}$$

In forced convection regime caused by the wind effect, i.e., $Gr^i/Re^{i^2} \ll 1$, Bejan [12] defined two internal convective heat transfer correlations depending on laminar or turbulent regime.

For a laminar flow ($Re^i_m > 2300$), the below equation is used where d is the thickness in m:

$$Nu_{cav-for}{}^i_m = 3.66 + \frac{0.0688\,\frac{d_{cav}}{mdy}Re^i_m Pr^i_m}{1+0.04\left(\frac{d_{cav}}{mdy}Re^i_m Pr^i_m\right)^{2/3}} \quad (22)$$

For a turbulent regime ($Re^i_m < 2300$)

$$Nu_{cav-for}{}^i_m = 0.0296 Pr^{i\ 1/3}_m Re^{i\ 4/5}_m \quad (23)$$

In the case of mixed convection regime, i.e., $Gr^i/Re^{i2} \approx 1$, the correlations for forced and natural convection are combined as:

$$Nu_{cav-mix} = \sqrt[3]{Nu^3_{cav-for} + Nu^3_{airgap-nat}} \quad (24)$$

Air temperature and thermal properties of the air in the air gap

The energy balance of air in the air gap depends on the mass flow rate M in kg/s and can be expressed:

$$h^i_{c,cav,Ins_m}\left(T^i_{T_{N,m}} - T^i_{cav_m}\right) + h^i_{c,cav,Ins_m}\left(T^i_{Ins_{1,m}} - T^i_{cav_m}\right) = M^i_m c^i_{p_{cav_m}} \frac{dT_{cav}}{dy} \quad (25)$$

By solving equation (25) and according to Mei et al. [45], the air temperature in the duct can be expressed as an exponential function of the gap height:

$$T^i_{cav_m} = exp\left(-\frac{(h^i_{c,cav,Ins_m} + h^i_{c,cav,T_m})Lm\Delta y}{M^i_m c^i_{p_{cav_m}}}\right)T^i_{inlet} + \left(1 - exp\left(-\frac{(h^i_{c,cav,Ins_m} + h^i_{c,cav,T_m})Lm\Delta y}{M^i_m c^i_{p_{cav_m}}}\right)\right)\frac{T^i_{T_{N,m}} + T^i_{Ins_{1,m}}}{(h^i_{c,cav,Ins_m} + h^i_{c,cav,T_m})} \quad (26)$$

where the inlet temperature at each time step is considered to be equal to the ambient air temperature [53] .

The thermal proprieties of the air are evaluated using the following correlations [75] at each time step as a function of the air temperature.

$$\rho^i_{cav} = 1.1614 - 0.00353\left(T^i_{cav} - 300\right) \quad (27)$$

$$k^i_{cav} = 0.0263 + 0,000074\left(T^i_{cav} - 300\right) \quad (28)$$

$$\mu^i_{cav} = \left[1.846 + 0.00472\left(T^i_{cav} - 300\right)\right] \times 10^{-5} \quad (29)$$

$$\beta^i_{cav} = 1/T^i_{cav} \quad (30)$$

$$c^i_{p_{cav}} = \left[1.007 + 0.0004\left(T^i_{cav} - 300\right)\right] \times 10^3 \quad (31)$$

Airflow rate and heat flow rate in the air gap

The airflow rate in the naturally ventilated air-space is driven by the stack effect and the wind effect [54]. Therefore, a model developed by Afonso and Oliveira [2] is used to determine the mass flow rate of the air in the cavity that is a function of the temperature of the airflow at the top and bottom openings:

$$M^i_m = \rho^i_m A_{in}\sqrt{\frac{2\ \beta^i_m\left(T^i_{cav,top} - T^i_{cav,bottom}\right)Lg + C_D V^{i2}_{air,ext}}{K_{f1} + K_{f2} + fr^i_m L/D_h}} \quad (32)$$

The opening coefficients are considered equal to K_{f1} = 0.5 andK_{f2} = 1.0 [9], and the wind pressure coefficient C_D is fixed to 0.25 [16] .

For laminar flow in a rectangular duct ($Re^i_m < 2300$), the friction factor fr is calculated as:

$$fr^i_m = \frac{96}{Re^i_m} \quad (33)$$

The friction factor can be calculated for turbulent flow [21] :

$$fr^i_m = \left(1.82\log Re^i_m - 1.64\right)^{-2} \quad (34)$$

The heat flow carried by airflow is a function of mass flow in the air cavity and its temperatures at the inlet and the outlet as shown below:

$$q_{cav}{}^i = M^i c^i_p (T^i_{cavM} - T^i_{cav_1}) \quad (35)$$

At the surface of the insulation material

At the surface of the insulating layer, the heat transfer mechanisms can be divided into convection with the air gap and radiation with the Tedlar layer, and the net heat flux is given by:

$$q^i_m = h^i_{c,cav,Rm}\left(T^i_{cavm} - T^i_{Ins1,m}\right) + h^i_{r,cavm}\left(T^i_{Ins1,m} - T^i_{TN,m}\right) \quad (36)$$

At the fiber plaster surface

At the internal surface of the fiber plaster, the convective and radiative heat transfer occurs between the surface and the indoor environment. The heat flux (in W/m^2) heat flux through the interior surface is a function of the indoor temperature, the surface temperature of the wall adjacent to the room, and the heat transfer coefficient in the indoor space [6] :

$$q^i_m = \left(T^i_{FPN,m} - T^i_{ind}\right)\left(h^i_{r,indm} + h^i_{c,indm}\right) \quad (37)$$

The convective heat transfer correlation between the indoor air and the internal surface of the wall is given by the following equation [9] :

$$h^i_{c,indm} = 1.31\left|T^i_{ind} - T^i_{FPN,m}\right|^{0.33} \quad (38)$$

The radiative heat transfers between the interior and the internal surface is given by:

$$h^i_{r,indm} = \sigma\varepsilon_{FP}\left(T^{i2}_{ind} + T^{i2}_{FPN,m}\right)\left(T^i_{ind} + T^i_{FPN,m}\right) \quad (39)$$

2.2.3. Transient responses of the wall assembly

The transient responses of the building envelope, including the time lag ($\varnothing$) and decrement factor (f), are evaluated using the exterior and interior surface temperatures [8] :

$$\varnothing = t_{T_{FP,max}} - t_{T_{Cl,ext,max}} \quad (40)$$

$$f = \frac{T_{FP,max} - T_{FP,min}}{T_{Cl,ext,max} - T_{Cl,ext,min}} \quad (41)$$

The abovementioned factors are essential for the analysis and interpretation of the heat storage capabilities of the building envelopes.

2.3. Weather data

For weather consideration, the weather data measured using a meteorological tower (GMX 300, Gill) in Lausanne, Switzerland, is used [27]. Measurements were done for the whole year of 2019 with 5-min intervals. Two sets of weather scenarios are used in this study; one for *typical days* and the other for *extreme days* in summer and winter. A comparison between typical and extreme days is provided for selected cases to analyze how the change in the weather conditions could affect the performance of the ventilated wall structures. To select the corresponding days from the weather data, the daily mean sol–air temperature is calculated using the following relationship [9] :

$$T_{sol-air} = T_{air,ext} + \frac{\alpha \cdot G}{h_{air,ext}} - \frac{\varepsilon \cdot \Delta R}{h_{air,ext}} \quad (42)$$

For vertical surfaces, it is assumed that $\varepsilon \cdot \Delta R = 0$, where ΔR is the extra infrared radiation factor in W/m^2, andα/h_c = 0.052 [9]. The typical days are determined using cumulative frequency analysis (with 50% percentile) of the daily sol–air temperatures [9]. The extreme days are determined as days when $T_{sol-air}$ is the maximum in summer and minimum in winter. Following the procedure described, December 14th and August 13th of 2019 are respec-

tively selected as the typical representative days in winter and summer. The selected extreme days in summer and winter are, respectively, December 30th and August 5th. The diurnal variation of weather conditions such as outdoor air temperature, wind speed, and vertical solar radiation are shown in Fig. 3 and Fig. 4. The outdoor temperatures are higher by 10 K in the extreme summer day compared to the typical summer days.

The vertical profile of wind velocity is calculated using equation (43), where Vz is the wind speed at the z height, V_m is the wind speed measured, l (0.21 for city area) and a (0.33 for city area) are the coefficients that take into account the topography and roughness of the surrounding environment [30]. As shown in Fig. 3 and Fig. 4, the wind speeds in the hottest and coldest days, however, are lower than the corresponding values in the typical days.

$$V_z = V_m \cdot l \cdot z^a \tag{43}$$

The horizontal solar radiation measured by the weather station is converted to the vertical direction to align with a west-oriented façade [22]. Indoor air temperatures are assumed to be equal to 21 °C in winter and 26 °C in summer [64] .

3. Validation

To validate the numerical model, different datasets are used for passive and active façade cases. The validation of the method for the passive façade is presented first, and the validation for the active façade is presented afterward.

3.1. Passive facade

The in-field measurements are performed using a shared research facility building prototype in the Smart Living Lab located in Fribourg, Switzerland, and the computational model for the passive façade is validated using the measured data on the non-glazed ventilated wall of the building prototype. It should be noted that the numerical model represents the same configuration as the test wall, which differs from what was described earlier for the passive facade. The external wooden façade of the wall structure is separated from the wall core with horizontal and vertical battens that create an air-space behind the cladding. The thermophysical properties of the layers of the wall assembly are summarized in Table 3.

A schematic view of the sensors placed on each wall section is depicted in Fig. 5. The temperature on each layer is monitored by using thermocouples (T-type with the accuracy of ± 0.1 °C, calibrated within the range of 10–50 °C) installed on the exterior and interior surfaces of the cladding, within the air-space, on the exterior surface of the insulation that is adjacent to the cavity, and on the interior surface of the wall core in the room. The sensors are positioned in three rows along with the height of the wall assembly to capture the vertical temperature distribution of each surface.

Omnidirectional anemometers (AirDistSys, Sensor-Electronic) with an accuracy of ± 0.02 m/s in the range of 0.05–5 m/s are employed. One is installed within the cavity to measure the speed of the airflow moving in the air-space. The sensor is positioned at the middle height of the air cavity and the center of the air gap width at a 45°angle from the side through the external cladding. This approach helps to avoid obstruction on the local environment in the vicinity of the measuring point. Moreover, it eliminates the sensor effect on the measurements since only the tip of the sensor, not the whole probe, is placed in the way of the airflow field in the air gap. The other anemometer is installed in the middle of the cladding to capture the outdoor airspeed with high resolution. A heat flux sensor (HFP01, Hukseflux) with an accuracy of ± 5% and a sensitivity of 60.89 μV/(W/m^2) is attached to the interior surface of the wall to measure the heat flux through the interior surface as shown in Fig. 5. All sensors are connected to a centralized data acquisition system (34972A, Keysight) with 0.1 °C of resolution and ±1 °C accuracy for temperature measurements. A weather station on the facade monitors outdoor conditions using an air temperature sensor (S-THB-M002, Onset), Davis® wind speed and direction sensor (S-WCF-M003, Onset), and silicon pyranometer for global horizontal irradiance (S-LIB-M003, Onset). The sensors in the weather station are connected to a micro station data logger (H21-USB, Onset). The data loggers are configured to record data at 1-minute intervals. It should be noted that although typically weather stations are installed on the roofs, we had the opportunity to place the instruments on the walls to monitor the local outdoor conditions with higher accuracy.

The west wall of the building prototype is modeled using the outdoor conditions and indoor temperature measured on a cloudy day with low solar radiation (March 15th) and a sunny day with high solar radiation (March 30th) in 2021, as shown in Fig. 6. By selecting these two days, the computational model could be evaluated under the wind-induced and buoyancy-induced dominant conditions.

The data collected by the sensors are compared with the results of the numerical model. Fig. 7a to Fig. 7e show the temperature profiles in the middle point on different surfaces. The uncertainty bands corresponding to the temperature measurements are also indicated in the plots. According to the results, the behavior of

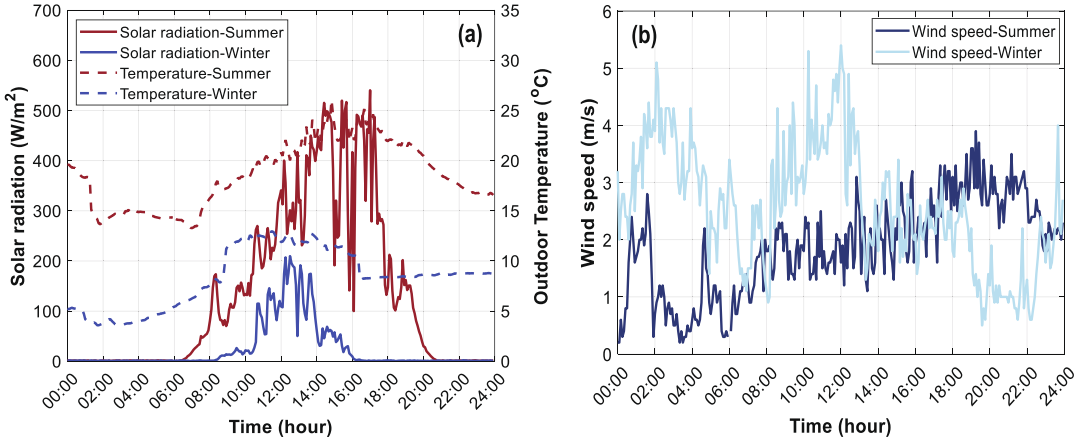

Fig. 3. Outdoor conditions for typical representative days (August 13th and December 14th of 2019) (a) outdoor air temperature and vertical solar radiation (b) wind speed.

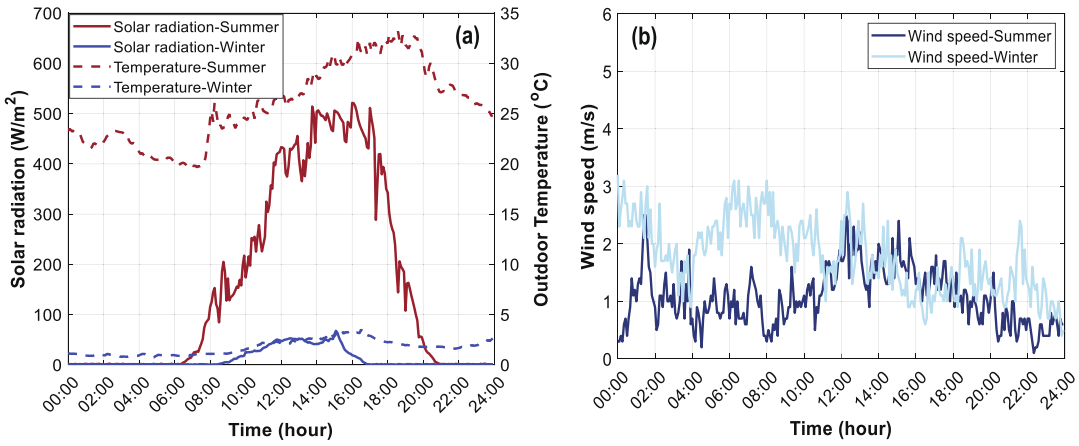

Fig. 4. Outdoor conditions for extreme days (August 5th and December 30th of 2019): (a) outdoor temperature and vertical solar radiation (b) wind speed.

Table 3
Properties of the wall assembly used for validation [13]

Material (exterior to interior)	d (m)	k (W/m · K)	c_p (J/kg · K)
Wooden cladding	0.024	0.10	1800
Air-space	0.070	–	–
Insulation polyurethane	0.180	0.03	1404
Timber hardwood	0.140	0.13	1600
Earth brick	0.050	0.79	1100
Jute coating	0.015	0.80	1450

the system is satisfactorily estimated by the numerical model. The difference between the simulated data and the measurements on all surfaces on a sunny day is higher compared to the cloudy day. This is mainly due to the effect of the instantaneous solar radiation on the outer surface of the external cladding that causes small fluctuations in the temperature profiles, as shown in Fig. 7a to Fig. 7d. These sudden fluctuations are not captured in the model due to the limitations in the interpolation method employed in the numerical calculations. Another source of error may be attributed to the uncertainties in the correlations used for the sky temperature and the sky radiation because of the numerical transformation of the cloud cover. According to Fig. 7e, the indoor condition is more stable compared to the outdoor, which yields smaller differences between the results predicted and the data measured on the interior surface compared to the other parts of the wall structure. The temperature of the airflow on top of the cavity is compared with the measurements in Fig. 7f to assess the results of the simulated model along with the height of the wall. The results confirm that the model can predict the temperature of the system along with the height of the wall with acceptable accuracy. Obviously, the presence of the battens in the way of airflow could affect the temperature distribution along with the height of the wall. Moreover, the probable recirculation zones in the entrance and exit area of the air-space close to the openings could have an impact on the airflow temperature. These aspects are not considered in the model and could explain small differences between the simulated and

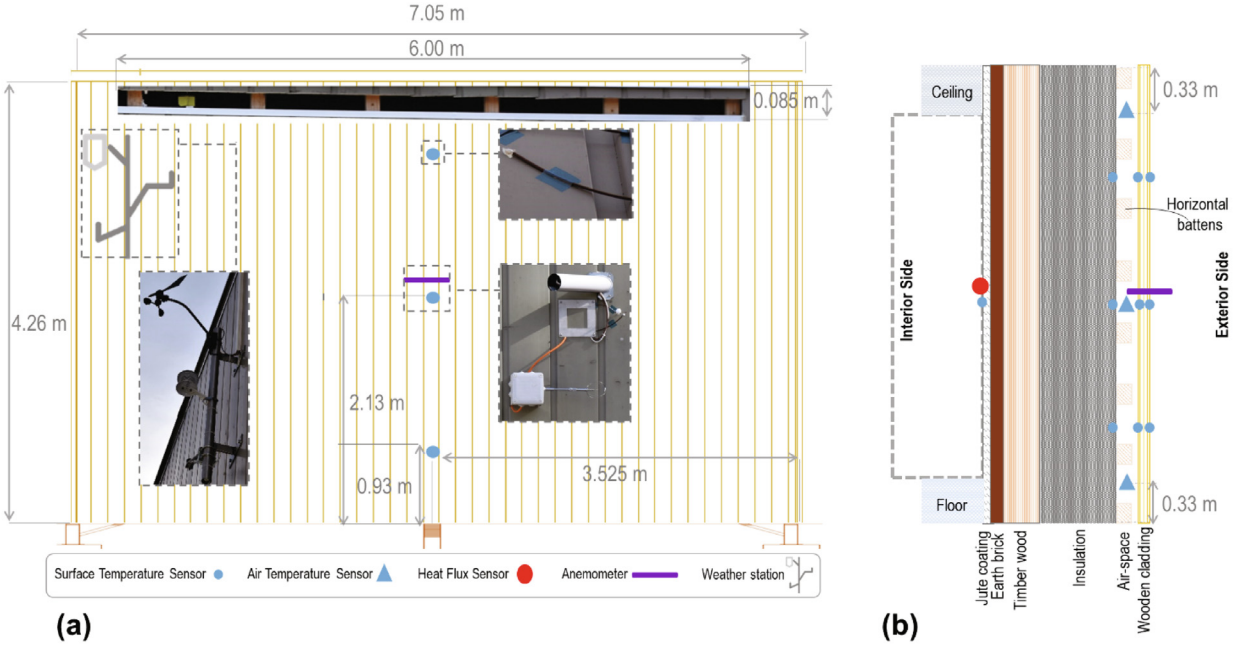

Fig. 5. Schematic of the sensors installed on different surfaces of the building prototype (a) Front view and (b) Cross-section.

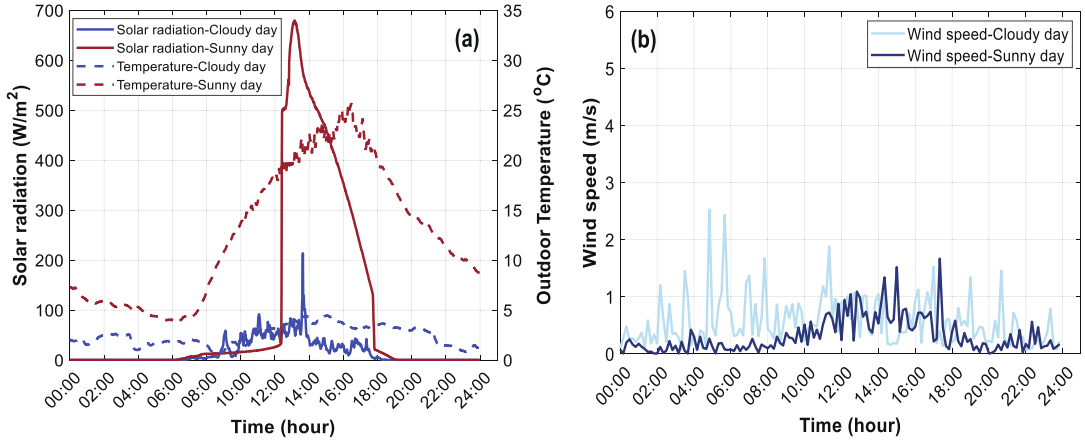

Fig. 6. (a) Outdoor temperature (°C) and vertical solar radiation (W/m^2) (b) Wind speed (m/s) measured during a cloudy day (March 15th) and a sunny day (March 30th) in 2021.

measured data. The plots in Fig. 7 depict that most of the time, the simulated results are overlapped with the uncertainty bands of the measurements, which means that the model can estimate the behavior of the system with adequate accuracy.

To quantify the numerical error, the Root Mean Square Error (*RMSE*) given in equation (44) and the relative Root Mean Square normalized Deviation (*RMSD*) using equation (45) are adopted [65,60,51] .

$$RMSE = \left(\frac{1}{m}\sum_{j=1}^{j=m}(T_{exp} - T_{sim})^2\right)^{1/2} \tag{44}$$

$$RMSD = \left(\frac{1}{m}\sum_{j=1}^{j=m}\left(\frac{T_{exp} - T_{sim}}{T_{exp}}\right)^2\right)^{1/2} \tag{45}$$

The statistical comparison of the data obtained is provided in Table 4. According to Table 4, the temperatures are well estimated by the computational workflow developed, and the mean relative deviation between the measured data and the simulated results is less than 1%. The mean error is less than 1.9 °C in all cases except for the exterior surface of the cladding that reaches 2.4 °C on a sunny day. However, the errors are still lower than the values reported for similar models in the literature. For instance, Marinosci et al. [43] predicted temperatures with errors of 5.0 °C. Seferis et al. [62] reported mean and maximum temperature prediction errors of 2.2 °C and 6.0 °C, respectively.

The amount of heat flux through the interior surface is shown in Fig. 8. The negative values in the plot mean that heat leaves the room. Based on the profiles shown, the heat flux is fairly well predicted by the numerical model. The values of *RMSD* for cloudy and sunny days are respectively 0.47% and 0.30%. The uncertainty in the thermo-physical properties of the wall layers is among the possible sources of error. The effects of the thermal bridges are not considered in the numerical simulation that could also cause the discrepancy in the results. Furthermore, the uncertainties in the correlations used for the convective and radiative heat transfer within the cavity and on the interior and exterior surfaces are the other sources of error. The 3-D effects through the width of the wall assembly, including the turbulences in the airflow within the cavity, also contribute to the errors.

Fig. 9 shows the profiles of the airspeed within the ventilated air gap measured and simulated for the cloudy and sunny days. Based on the results, the trend of the speed of the airflow has been predicted by the model in good agreement with the data measured. By ignoring the instantaneous upswings in the airspeed, the mean difference between the simulated and measured data is around 0.1 m/s, which is mainly due to the blockage and local perturbations in the airflow triggered by the presence of the horizontal and vertical battens in the cavity. The error could also be attributed to the assumptions used in equation (32).

3.2. Active facade

In order to validate the numerical simulation for the active façade, the results of the experimental measurements by Agathokleous and Kalogirou [3] are compared with the results of a similar model in that study simulated by employing the computational model. The experimental setup used is a naturally ventilated BIPV system test rig comprised of a polycrystalline PV module with dimensions 1640 × 992 × 4 mm^3. An air gap with 100 mm thickness separates the PV panel from the wall core. The experimental apparatus is exposed to a solar simulator under 800 W/m^2 of uniform and constant solar radiation for 160 min; then, the solar simulator is turned off to let the system cool down. During the experiments, it is observed that the temperature of the system was constant after the first 40 min, which includes the start-up of the solar simulator. Temperature sensors are installed on the PV panel to measure the surface temperature at the top, middle, and bottom of the module. Thermocouples are also placed at the bottom, middle, and top of the air gap. Fig. 10 shows the results of the simulation compared with the measured data (excluding the start-up time of the solar simulator) using the same conditions in the experiments. As can be observed from Fig. 10, the results simulated have the same trend as the data measured and are in good agreement.

Since the exact experimental data was not accessible, the maximum relative error between the simulated results and the measured data is determined to evaluate the results of the simulation [4]. The relative errors are obtained using equation (46), and the maximum values are provided in Table 5. The relative error is calculated based on the difference between the simulated and the measured temperature values in Kelvin since it only makes sense when measured on a scale that has a true meaningful zero [67] .

$$RE(\%) = \left|\frac{T_{exp} - T_{sim}}{T_{exp}}\right| \times 100 \tag{46}$$

According to Table 5, the maximum relative error does not exceed 1.74%, which confirms that the model can predict the temperatures of the system within an acceptable range in good agreement with the measurements. The temperature profile simulated

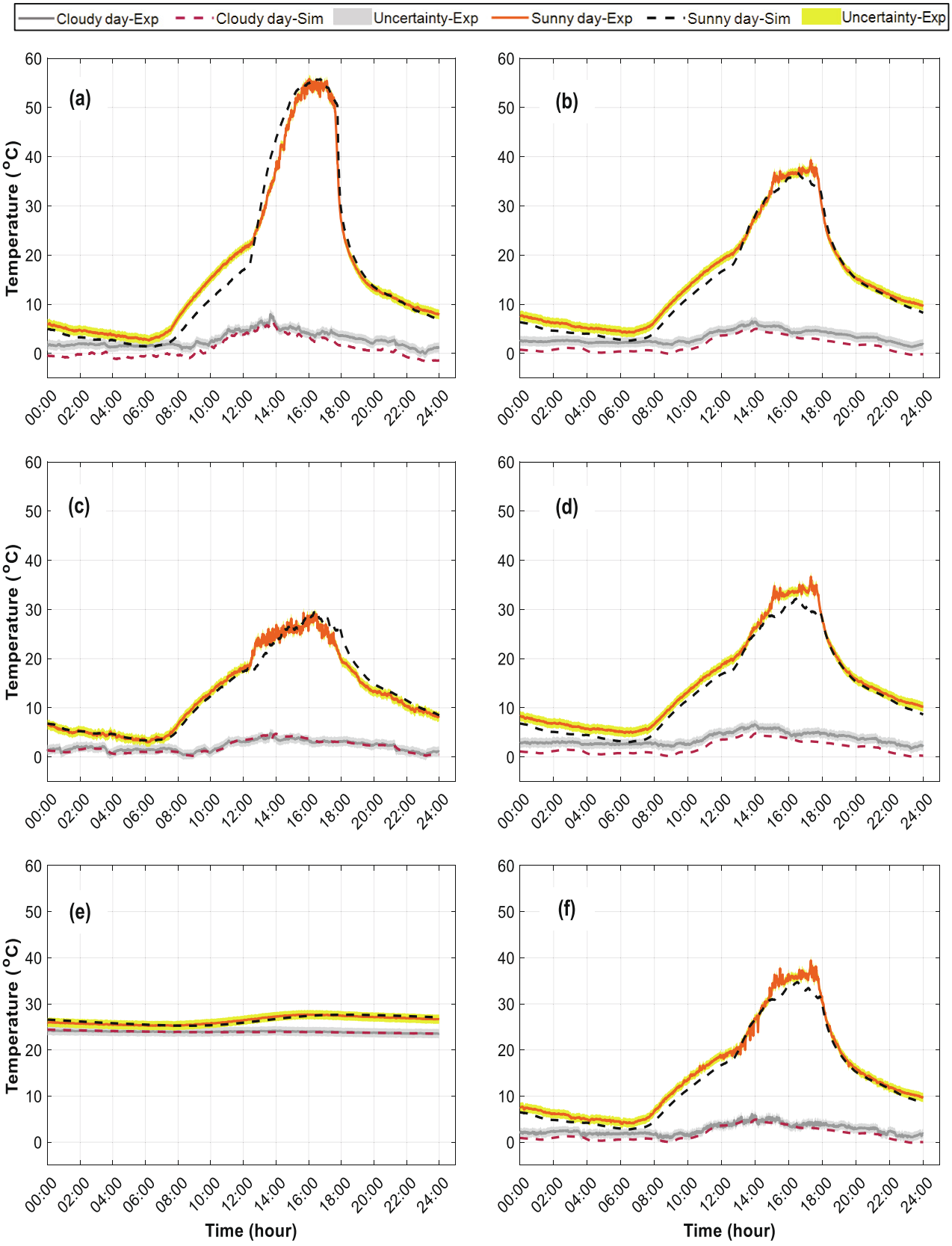

Fig. 7. Temperature profiles in the middle height modeled (dashed lines) and measured (solid lines) during the cloudy day and the sunny day (a) Exterior surface of the façade, (b) Interior surface of the façade, (c) Inside the air-space, (d) Insulation surface adjacent to the cavity, (e) Interior surface of the Jute coating, (f) Top of the cavity.

Table 4
Statistical comparison between the computed and measured temperatures.

Surface temperature	Cloudy day		Sunny day	
	RMSE (°C)	*RMSD* (%)	*RMSE* (°C)	*RMSD* (%)
$T_{cl,ext}$	1.8	1.00	2.4	0.16
$T_{cl,int}$	1.6	0.59	1.7	0.15
T_{cav}	0.4	0.13	1.4	0.01
$T_{ins,ext}$	1.7	0.54	1.9	0.15
$T_{jc,int}$	0.1	0.01	0.3	0.01
$T_{cav,top}$	1.0	0.45	1.8	0.14

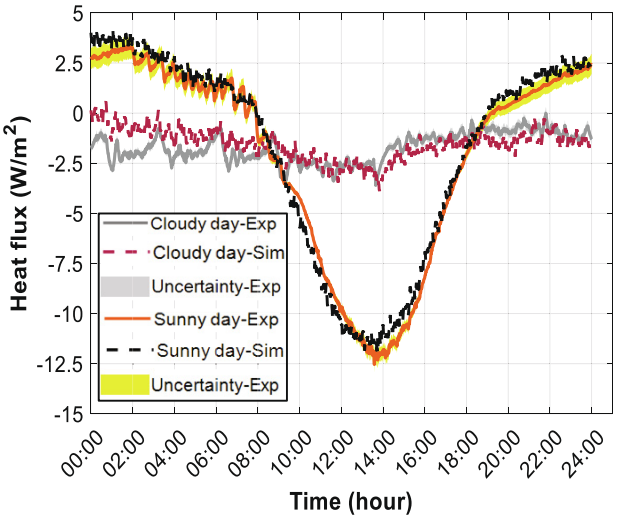

Fig. 8. Profiles of the heat flux through the interior surface in the middle height simulated (dashed lines) and measured (solid lines) during the cloudy day and the sunny day.

at the bottom of the PV surface differs up to 5 °C compared to the measurements (Fig. 10). As described by Agathokleous and Kalogirou [4], the small difference between the results simulated and the data measured could be attributed to the difference in the correlation used for the Nusselt number in the model and the actual value in experiments.

Based on the abovementioned results in section 3.1 and section 3.2, despite the small differences observed in a few cases between the results simulated and the data measured, the numerical model can be relied upon to adequately capture the 2-dimensional thermal behavior of the entire wall structure in both passive and active ventilated facades. It should be highlighted that the acceptable agreements between the model and the measured data are obtained after performing several tests using various correlations and empirical equations available in the literature to find the best match with the experimental measurements. Therefore, further analyses are performed using the computational model to assess the performance of the ventilated wall structure under various conditions.

4. Results

The results of the scenarios specified in section 2.1 are presented in this section. The temperature distribution on the surfaces of the wall structure, heat flux passing through the wall core, airflow moving through the air-space, heat flow removed from the cavity, the electrical efficiency of the active facades, and the transient responses of the building envelope are examined in section 4.1 to section 4.6 for different scenarios using the weather data of typical representative days in summer and winter. Thereafter, the weather data is changed to the extreme conditions, for selected scenarios and compared with the results for typical days. The abbreviations mentioned in the text and indicated in the Figures are described in Table 2.

4.1. Temperature distribution within the wall structure

The temperature profiles in the middle point on the exterior and interior surfaces of the external cladding, the airflow in the air-space, the insulation surface adjacent to the cavity, and the

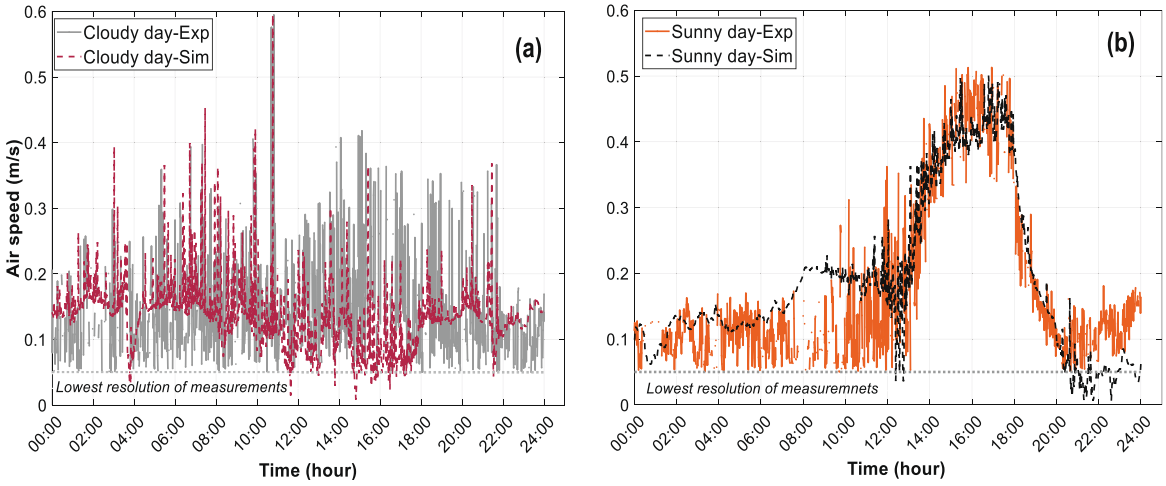

Fig. 9. Profiles of the airflow speed in the air-space in the middle height simulated (dashed lines) and measured (solid lines) during (a) cloudy day and (b) sunny day.

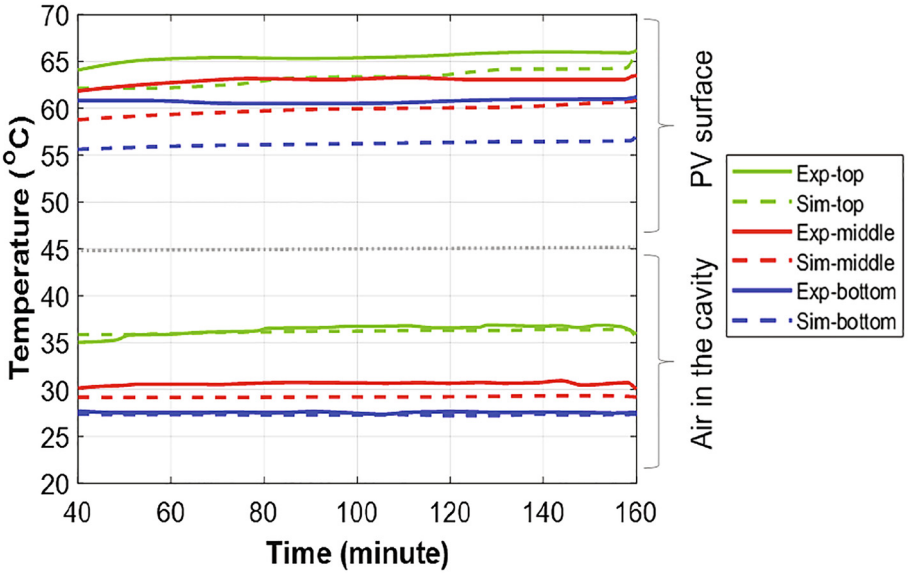

Fig. 10. Experimental data (solid line) and simulated results (dashed line) of the air temperatures in the cavity and PV surface temperature at the top (black), middle (red), and bottom (blue). (For interpretation of the references to colour in this figure legend, the reader is referred to the web version of this article.)

Table 5
Maximum relative error between the computed and measured temperatures.

Temperature	$T_{PV,top}$	$T_{PV,middle}$	$T_{PV,bottom}$	$T_{cav,top}$	$T_{cav,middle}$	$T_{cav,bottom}$
Error	1.04%	1.57%	1.74%	0.19%	0.64%	0.49%

interior surface of the wall core adjacent to the indoor space is shown in Fig. 11. The results during the typical days in summer and winter are provided for passive and active ventilated facades with two cavity depths (45 mm & 110 mm) and having lightweight and heavyweight wall cores. The results of cases with the presence or absence of reflective insulation in the cavity are combined considering the thickness of the cavity equal to 45 mm or 110 mm.

4.1.1. Effect of the cladding type

The profiles presented in Fig. 11 indicate that the surface temperatures of the wall assembly with the active façade in winter are always higher compared to the passive cladding. On a typical summer day, however, the surface temperatures of the passive cladding became higher than the active façade in a short period at night (between 1:00 to 3:00) and afternoon (after around 17:40). The outdoor temperature and the solar radiation in these periods are comparatively lower than the rest of the day (see Fig. 3), and apparently, the active façade with the PV panel has been more affected compared to the passive cladding. The layers used in the PV module have different thermo-physical properties compared to the passive cladding. This results in having more interactions with the outdoor conditions and being more influenced when the outdoor conditions change during the day. The fluctuations shown in the temperature profiles for the passive façade could also be justified for the same reason. The maximum temperature difference between the active and passive façades is 13.6 °C that occurs on the interior surface of the cladding in the *H-TS110* case.

4.1.2. Effect of the thermal inertia of the wall core

According to the results, excluding the temperature of the interior surface of fiber plaster adjacent to the indoor space, the temperature distribution of the other surfaces shown in Fig. 11 is almost identical in passive and active facades for the lightweight and heavyweight wall cores. However, the interior surface temperatures of fiber plaster are different due to the type of the wall core contribution to the problem. Although during the typical day in winter the interior surface temperature of the *L-TW* case is always lower than the *H-TW* case in both cladding types, it could be higher after 15:00 in the *HA-TS* case and after 17:00 in the *HP-TS* case. This could be attributed to the difference in the conductivity and thermal capacity of the materials used in the wall cores. The effect of these parameters is more pronounced when the entire structure is exposed to high solar radiation during the summer day.

4.1.3. Effect of the seasonal variation

The temperature fluctuations on the surfaces of the wall structure are more noticeable on the typical summer day compared to the typical winter day. This is due to the instantaneous variations in the solar radiation that is more evident in summer. Considering the plots shown in Fig. 11, the temperature of the exterior surface of cladding in the case of the active façade varies within the range of 13.4 °C to 44.6 °C in summer and within the range of 3.3 °C to 18.3 °C in winter. The ranges are lower in the case of the passive cladding (13.2 °C to 35.8 °C in summer and 2.6 °C to 15.6 °C in winter). Comparing the values with the outdoor temperature in the typical days (Fig. 3), it can be observed that the exterior surface temperature of the claddings could become up to 20 °C (active façade) and 10 °C (passive façade) higher than the outdoor ambient temperature in the typical summer day. The corresponding values are lower when the temperatures on the interior surface of cladding (with a maximum value of 44.2 °C) and the exterior surface of insulation (with a maximum value of 36.8 °C) are considered. The airflow in the ventilated air-space passes through the cavity with a lower temperature compared to the adjacent surfaces (up to 14 °C in summer and 4 °C in winter) and removes the accumulated heat between the external cladding and the wall core that consequently reduces the cavity wall temperatures.

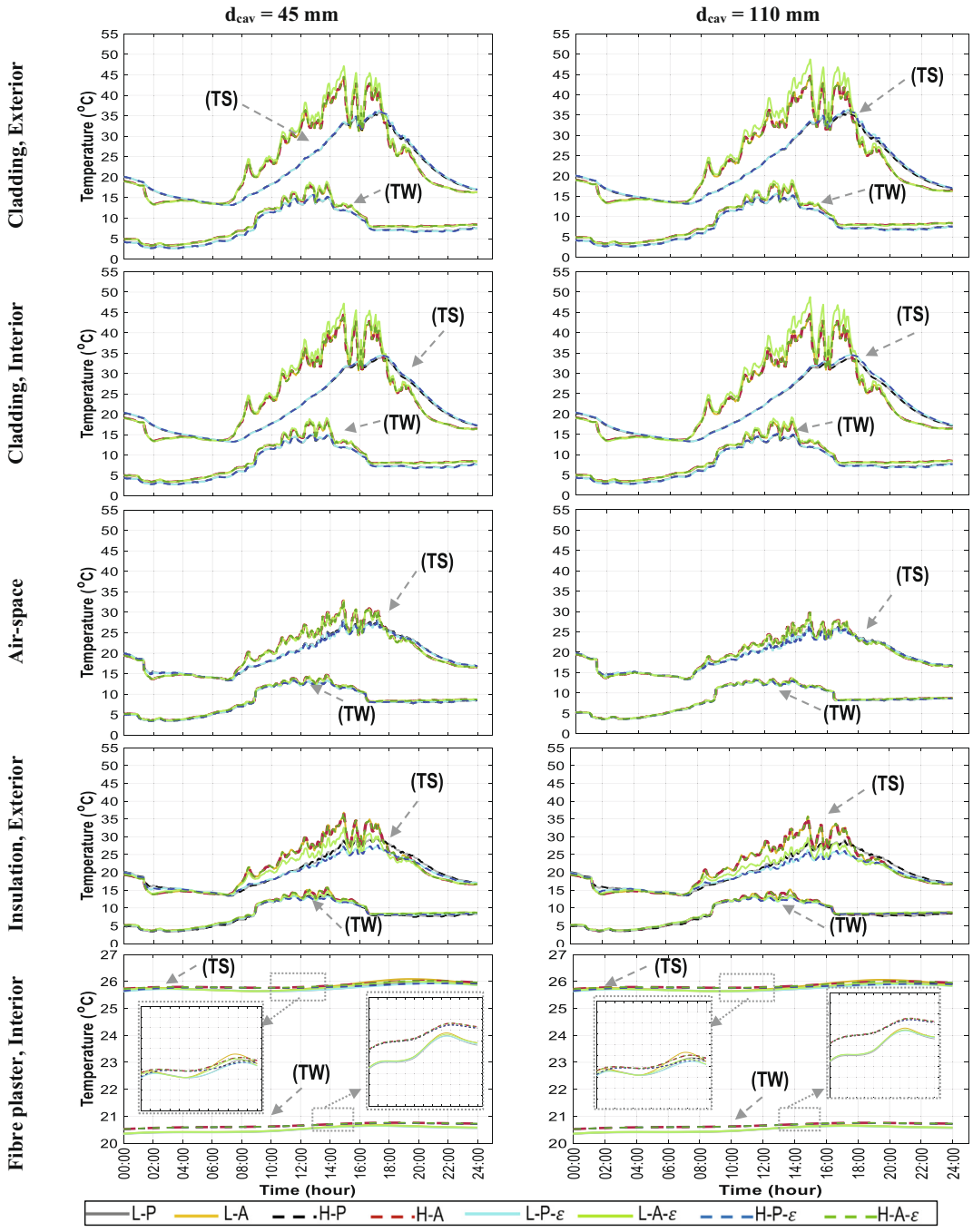

Fig. 11. Temperature profiles at the middle point on different surfaces in the wall structure during typical outdoor conditions (refer to Table 2 for abbreviations). Summer cases (TS) are upper curves, and winter cases (TW) are lower curves.

4.1.4. Effect of the cavity thickness

Based on the results, the increase in the cavity thickness reduces the temperature of the interior surface of cladding, the air-flow temperature in the air-space, and the exterior surface of the insulation. These observations are due to the increase in the air-flow rate passing through the cavity with a higher thickness (see section 4.3), which consequently reduces the surface temperatures. The temperatures become lower in the air-space (up to 2.5 °C) in both passive and active facades when the thickness of the cavity is increased from 45 mm to 110 mm. Similar results for a ventilated BIPV system are provided by Lau et al. [40], which show a 1 °C drop in the PV surface temperature by enlarging the thickness of the cavity from 45 mm to 110 mm. Comparing the results provided in Fig. 11, the change in the cavity thickness has a negligible effect on the temperature of the interior surface of the wall assembly.

4.1.5. Effect of the presence of reflective insulation

In terms of the effect of the reflective insulation placed on the cavity surface, the temperatures of the exterior and interior surfaces of the cladding are higher for the lightweight wall core compared to the heavyweight wall core. In contrast, the exterior surface temperature of insulation and interior surface temperature of fiber plaster become lower in the case of the lightweight wall

core. The differences are more pronounced in the wall structure with the active façade during the solar exposure of the cladding in summer. These observations reveal the effect of the presence of the reflective insulation on the temperature change of the entire wall assembly. The maximum temperature difference occurs in the active façade between the *L-TS45* and *H-TS45* cases, and the values are respectively equal to 3.9 °C, 4.0 °C, and 6.0 °C for the exterior surface of cladding, the interior surface of cladding, and the exterior surface of the insulation. Considering the temperature of the airflow in the air-space, the difference between the active and passive facades becomes lower when the thickness of the cavity increases from 45 mm to 110 mm. A similar trend can be observed for the temperature of the exterior surface of the insulation layer. Comparison of the results for reflective insulation cases shown in Fig. 11 reveals that using reflective insulation in the cavity can increase the temperature of the exterior and interior surfaces of the active cladding up to 2.5 °C and 2.6 °C in case of the lightweight wall core and cavity thickness equal to 45 mm. By enlarging the air gap, the increase in the aforementioned temperatures becomes 3.9 °C and 4.1 °C respectively. The presence of the reflective insulation decreases the temperature of the exterior surface of the wall core by 4.2 °C and 6.0 °C in the same wall assembly incorporating cavities with 45 mm and 110 mm thickness, respectively. The corresponding values are relatively low on the typical day in winter and reach up to 1.5 °C.

Regarding the comparison of the temperature distribution between the passive and active facades, similar trends as the cases without using reflective insulation can be observed. The maximum temperature difference between the active and passive façades is 17.3 °C that occurs on the typical summer day on the interior surface of cladding when the thickness of the air gap is 110 mm, and the lightweight wall core is used in the assembly. The results reveal that the presence of the reflective insulation could increase the temperatures on the same surface by up to 17.8 °C, which is 4.2 °C higher compared with the case without using reflective insulation in the air gap.

The temperature of the exterior surface of cladding in the case of the active façade varies within the range of 13.3 °C to 48.7 °C in summer and within the range of 3.3 °C to 19.1 °C in winter. The ranges are lower in the case of the passive cladding (13.2 °C to 36.4 °C in summer and 2.6 °C to 15.7 °C in winter). Therefore, the presence of the reflective insulation in the cavity slightly increases the temperature range of the surfaces in both typical days in summer and winter compared to the cases when no reflective insulation is used in the air-space. The reason for the abovementioned observations in the results is the lower emissivity of the surface caused by the reflective insulation, which contributes to the radiation heat transfer between the cavity walls and consequently affects the temperature of the surfaces.

4.2. Heat flux through the interior surface

The profiles of the heat flux through the indoor surface for various scenarios simulated are shown in Fig. 12. The negative values mean that heat leaves the indoor space (detailed in equation (37)). Based on the results, the absolute values of the heat flux are almost always greater in the lightweight than in the heavyweight wall cases. Only within a few hours during the typical summer day (from 15:00 to 21:00), the heat flux through the interior surface becomes greater in the heavyweight compared to the lightweight structure. This is mainly due to the temperature distribution on the interior side of fiber plaster, as discussed in section 4.1. The maximum difference between the amplitudes of the heat flux during the day for the lightweight structure reaches 3.4 W/m^2, while it is 2.2 W/m^2 in the heavyweight assembly. Comparing the wall structures with passive and active facades, it can be seen that the heat flux leaving the indoor space is always higher in the case of passive cladding. There is also a shift of around 2 h in the maximum heat flux leaving the indoor space in summer comparing the active and passive facades. In winter, however, the difference in the amount of heat flux between the two cladding types is not considerable.

According to the results, the heat flux most of the time leaves the indoor space during both typical days in summer and winter. The set point temperature fixed for the indoor space is higher than the outdoor air temperature, which consequently results in heat flux leaving the interior side of the building even on the typical summer day. Only within a few hours during the summer day (from 17:00 to 21:00), the temperature of the interior surface of fiber plaster becomes greater than the indoor temperature and heat enter the room. The maximum value of the heat leaving the indoor space in summer is 2.8 W/m^2, while it is higher on the typical winter day and reaches 4.8 W/m^2. According to the plots in Fig. 12, increasing the thickness of the cavity has a negligible effect on the amount of heat flux if reflective insulation is not placed in the air gap. However, by reducing the emissivity of the cavity surface and using a layer of reflective insulation, the amount of heat flux becomes greater in the case of *LA-TS*. Moreover, the use of reflective insulation can reduce the difference in the heat flux through the interior surface between the *LP* and *LA* cases.

The results can also be compared in terms of the energy-saving rate of the wall assembly (Patania et al., 2010) by calculating the difference between the heat flux through the interior surface in different conditions. According to Fig. 13, the maximum energy saving rate could reach up to 50% in summer and 30% in winter, comparing lightweight and heavyweight wall structures (between 6:00 to 10:00). The preference for thermal mass in the wall core to decrease the heat gain (or increase the heat loss) varies during the typical summer day. In winter, however, it is always desired to use

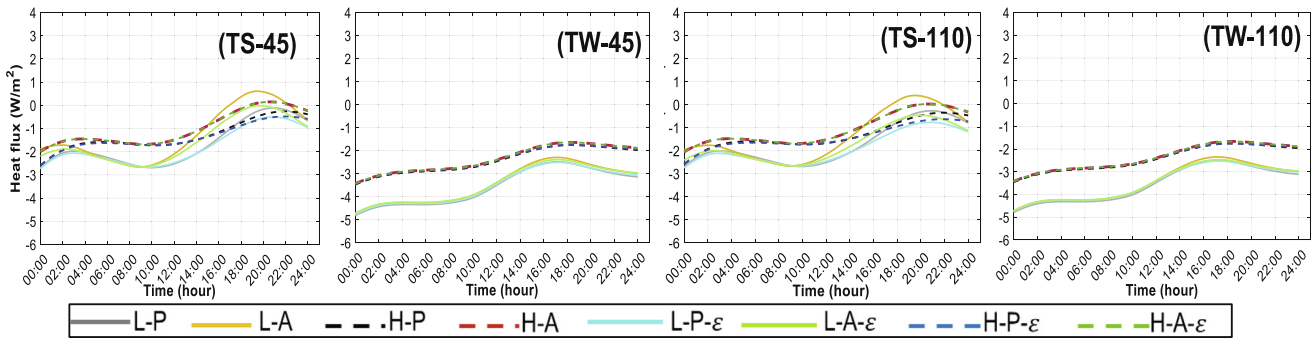

Fig. 12. Profiles of the heat flux through the interior surface at the middle point in the wall during typical outdoor conditions (refer to Table 2 for abbreviations).

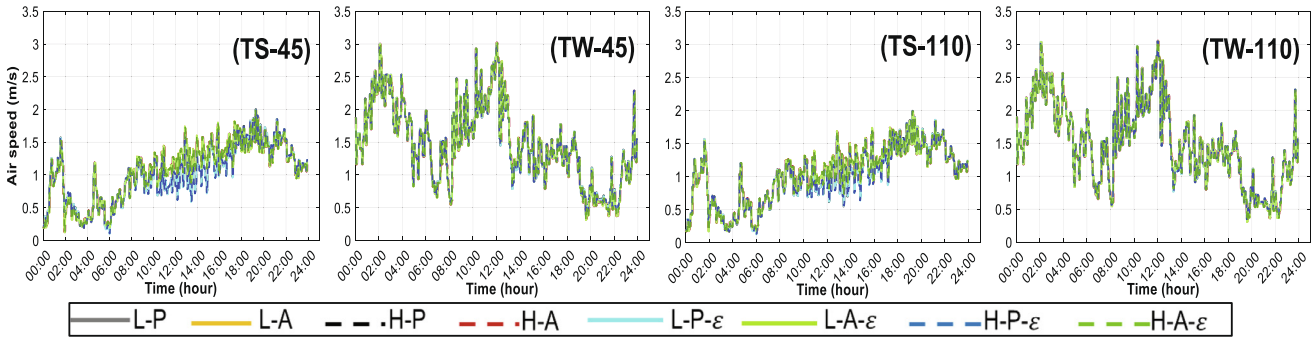

Fig. 13. Profiles of the airspeed at the middle point in the air-space during typical outdoor conditions (refer to Table 2 for abbreviations).

a wall with high thermal mass to lower the heat loss through the wall structure.

4.3. Airflow in the air-space

The profiles of the speed of airflow moving in the ventilated air-space are shown in Fig. 13. There is no considerable difference between the lightweight and heavyweight structures. This observation was expected since the airflow in the cavity is driven by the stack effect and wind effect, which are a function of the type of the external cladding and are independent of the thermal mass of the wall assembly. The speed of the airflow in the air gap for both wall cores in the *A-TS* case is 0.8 m/s higher compared to the *P-TS*. The difference is 1.2 m/s during the typical day in winter. This is mainly due to the buoyancy effect that is caused by the higher temperature of the airflow triggered by the higher temperature of the interior surface of the cladding in case of using an active façade. The profiles of the airspeed in all cases generally follow the wind speed profiles shown in Fig. 3. The higher wind speed during the typical winter day most of the time results in greater airspeeds in the cavity compared to the typical summer day. The airspeed increases by up to 0.1 m/s if the thickness of the cavity enlarges from 45 mm to 110 mm. Based on the results, the effect of the presence of the reflective insulation on the airspeed in the air-space is negligible.

4.4. Heat flow passing through the cavity

The profiles of the heat flow removed from the air-space are shown in Fig. 14. The negative values in the mornings for the case of passive facades indicate that the temperature of the airflow at the top of the cavity is lower than the temperature at the bottom; thus, the heat direction is downward (equation (35)). As discussed in section 4.3, the airflow speed does not change by varying the thermal mass of the wall. The results in section 4.1 also revealed that the temperature difference in the air-space between the two types of walls with low and high inertia is not significant when the reflective insulation is not used. Therefore, the thermal mass of the wall core has no significant effect on the heat flow in the air gap bounded with high emissivity surfaces. By using a layer of reflective insulation in the air-space (i.e., decreasing the emissivity of the cavity surface adjacent to the wall core), the capacity of heat removal from the cavity increases when the wall core has higher thermal inertia. The maximum difference in the heat removed occurs between the *LP* and *HP* cases are respectively equal to 18.3 W/m^2 and 34.8 W/m^2 in the smaller cavity and wider cavity.

The heat flow removal from the cavity is mostly higher in the active façade compared with the passive cladding. This is due to the higher airspeed in the cavity and also the higher temperature of the external surface in the active façade when it is exposed to solar radiation. The heat flow becomes higher after 17:00 during the typical summer day in the passive cladding compared to the active façade, which is related to the higher temperature of the cavity surfaces (see section 4.1) and also the higher temperature gradient in the airflow between the top and bottom openings in this case. The maximum difference in the capacity of heat removal between the *HP-TS45* and *HA-TS45* cases is 640.8 W/m^2. By enlarging the air-space to 110 mm, the difference becomes equal to 929.8 W/m^2. By reducing the emissivity of the cavity surface, the corresponding values slightly increase to 659.0 W/m^2 and 961.2 W/m^2.

The effect of the outdoor condition on the heat flow removed from the air-space is significant. The maximum values corresponding to the *HA-TS45* and *HA-TS110* cases are respectively equal to 879.2 W/m^2 and 1161.3 W/m^2. The values remain almost identical in the case of reduced emissivity of the cavity surface. In winter, however, the capacity of heat removal from the air gap decreases

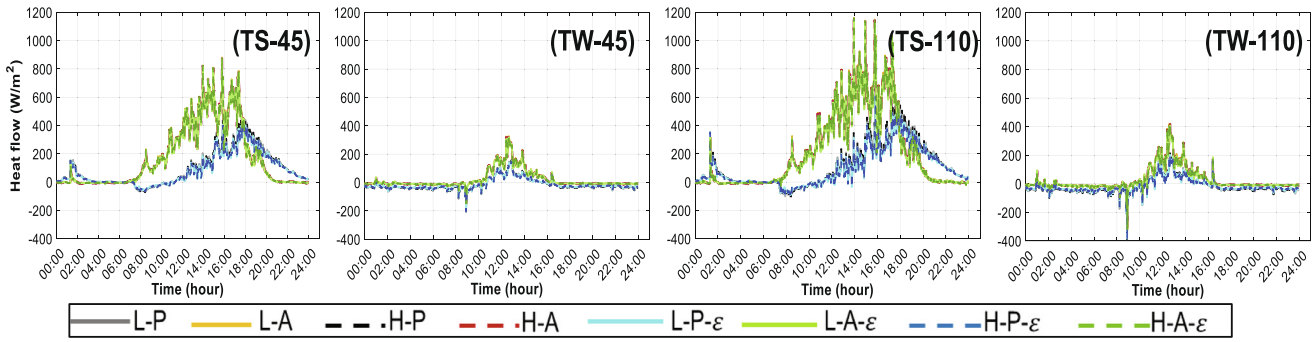

Fig. 14. Profiles of the heat flow removed from the air-space during typical outdoor conditions (refer to Table 2 for abbreviations).

to 326.8 W/m^2 and 420.9 W/m^2 for the smaller and wider cavities, respectively. These observations reveal the importance of the effect of solar radiation on the temperature gradient within the cavity, which consequently improves dissipating the accumulated heat from the ventilated air-spaces. It should be noted that the magnitude of negative values shown on plots in Fig. 14 is greater during the typical winter day (in particular between 8:00 to 10:00) compared to the typical summer day. The relatively high wind speed drives the air into the air-space at a temperature that is higher than the air temperature at the top of the cavity that is due to the low solar flux in this particular morning period, which causes a negative temperature gradient of the airflow in the air gap. Therefore, the heat flow exits from the bottom of the air gap, and the flow direction is downward.

4.5. Electrical efficiency of the PV panel

The profiles of the electrical efficiency of the PV panel during the typical summer day for hours when the system is exposed to the Sun are presented in Fig. 15. The profiles are not shown for the cases in the winter period, since the temperature of the PV panel (see Fig. 11) is always lower than the reference temperature shown in equation (16), and the efficiency has been remained equal to the reference efficiency (i.e., 12%). The results indicate that the electrical efficiency of the module is almost identical for the LP-TS and HP-TS cases. This is due to the low difference in the surface temperature of the PV façade in lightweight and heavyweight walls. Reducing the emissivity of the cavity surface, however, causes a slight decrement in the efficiency of the PV panel if the lightweight wall core is used. Based on the results, increasing the thickness of the air-space could slightly increase the electrical efficiency of the PV module, which is due to the decrease in the surface temperature of the active façade.

4.6. Transient responses of the wall assembly

In this section, the transient responses of different wall assemblies are analyzed. The results of the simulations for lightweight and heavyweight wall structures having passive and active facades are provided in Fig. 16. According to the results, the time lags of the heavyweight structures are higher compared to the lightweight walls, as expected. The difference in the values of ∅ between the *HP-45* and *LP-45* during the typical summer day and winter day are respectively 1.05 h and 1.09 h. These values become 1.00 h and 1.07 h for similar wall structures with active façade. By increasing the thickness of the cavity to 110 mm, the value for each wall structure slightly decreases in summer and slightly increases in winter; however, the difference between the lightweight and heavyweight wall assemblies remains almost identical.

By incorporating reflective insulation in the air-space, the time lags slightly decrease in summer (up to 0.10 h) and slightly increase in winter (up to 0.12 h). As shown in Fig. 16, replacing the traditional external cladding with the BIPV façade increases the ∅ value of the entire wall structure during the typical summer day and decreases the delay during the typical winter day. These observations could be justified with the change in the temperature distributions on the exterior and interior surfaces provided in section 4.1. The maximum difference in the time lag between the *LP-45 ε* and *LA-45 ε* cases reaches 1.74 h in summer and 1.10 h in winter. By increasing the thickness of the air gap, the corresponding values become 2.04 h in summer and 1.13 h in winter. Comparing two identical wall assemblies, the values of ∅ for passive cladding are lower during the typical day in summer compared to winter. For the active façade, however, the values become greater when the typical day changes from summer to winter. The lowest time lag ∅ corresponds to the *LP-TS110 ε*, while the highest value corresponds to the *HP-TW110 ε*.

Regarding the decrement factor *f*, the results reveal that the maximum value during the typical days in summer and winter are 0.016 and 0.023, respectively. The maximum difference between the *LP-45* and *HP-45* are 0.002 and 0.05 in summer and winter, respectively. The *f* decreases in both seasons by replacing the passive cladding with an active façade. Furthermore, increasing the thickness of the cavity and reducing the emissivity of the cavity surface decrease the decrement factor in all cases. The maximum *f* corresponds to the *LP-TW45* and *LP-TW110*, while the minimum value corresponds to the *HP-TS110 ε*.

Effect of the outdoor conditions

The impacts of the weather data on the thermal and electrical performance of the passive and active ventilated wall structures are examined in this section. The *L-E45* and *H-E45* cases are selected for simulations. The temperature profiles at the middle point on the exterior surface of cladding, within the air gap, and

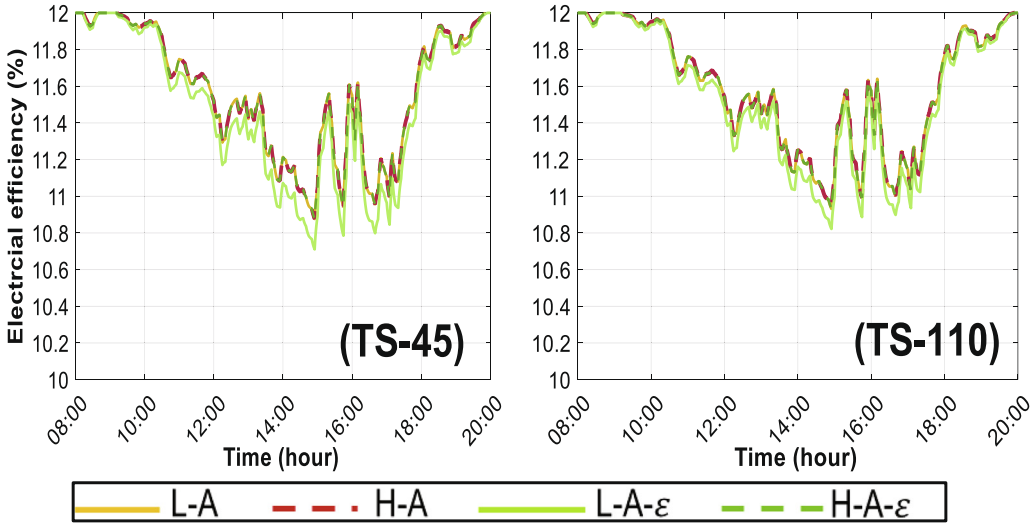

Fig. 15. Profiles of the electrical efficiency of the PV panel during typical outdoor conditions (only the period of the exposure to the solar radiation is shown, refer to Table 2 for abbreviations).

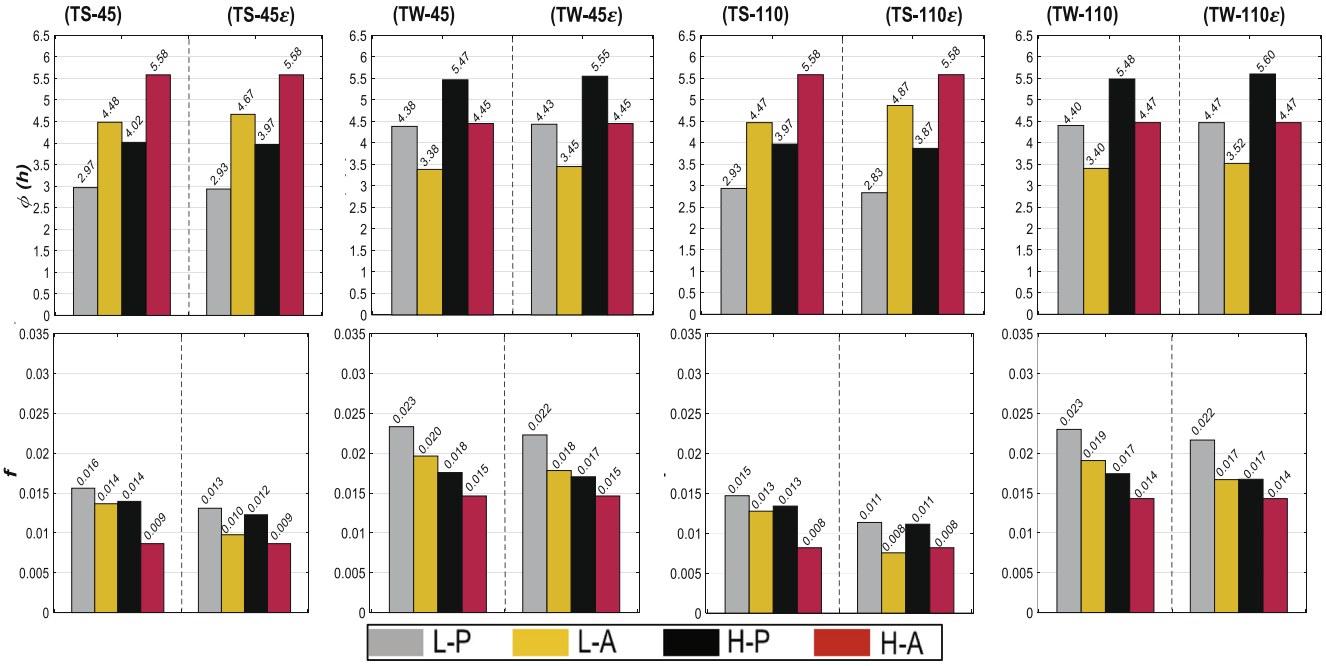

Fig. 16. Time lag (first row) and Deceremnt factor (second row) of the wall structure during typical outdoor conditions (refer to Table 2 for abbreviations).

on the interior surface of fiber plaster during the extreme outdoor conditions are shown in Fig. 17.

4.6.1. Temperature distribution within the wall structure

The results reveal that the temperature of the exterior surface of cladding in the *LP-ES45* and *LA-ES45* cases could respectively reach up to 52.6 °C and 47.5 °CCompared with the typical day in summer, the temperature has increased by about 8.0 °C and 12.0 °C for the active and passive facades. The maximum exterior surface temperatures in winter for the passive and active facades are respectively 2.7 °C and 5.7 °C, which are 13 °C lower compared with the results in the typical day. The temperature of the airflow in the air-space also has a 10 °C difference with the corresponding values in the typical days in summer and winter. Comparing the temperatures on the interior side of fiber plaster with the results shown for the typical days reveal that the temperature is shifted for 0.4 °C in summer. Moreover, the amplitudes of the temperature profiles in both extreme days are reduced compared to the typical days. The temperature on the interior surface of the wall becomes greater than the set point temperature in summer (26 °C) for a longer period compared to the typical summer day. The higher outdoor temperature and solar flux during the extreme summer day and the lower values during the extreme winter day are the original cause of the aforementioned observations.

4.6.2. Heat flux through the interior surface

Profiles of the heat flux through the indoor surface during extreme outdoor conditions are shown in Fig. 18. The results indicate that the maximum difference between the amplitudes of the heat flux in both cladding types for the *L-ES45* case reaches 4.0 W/m^2 that is greater compared to the typical day. The maximum heat that leaves and enters the indoor space in summer is respectively 2.0 W/m^2 and 3.2 W/m^2. The maximum value of heat that leaves the indoor space in winter reaches 5.5 W/m^2. Comparing the results with the typical days, it can be observed that the heat escaping the indoor space becomes greater in winter. This is due to the higher temperature difference between the indoor and outdoor spaces in the extreme day compared to the typical day. The time duration on the summer day that heat enters the room

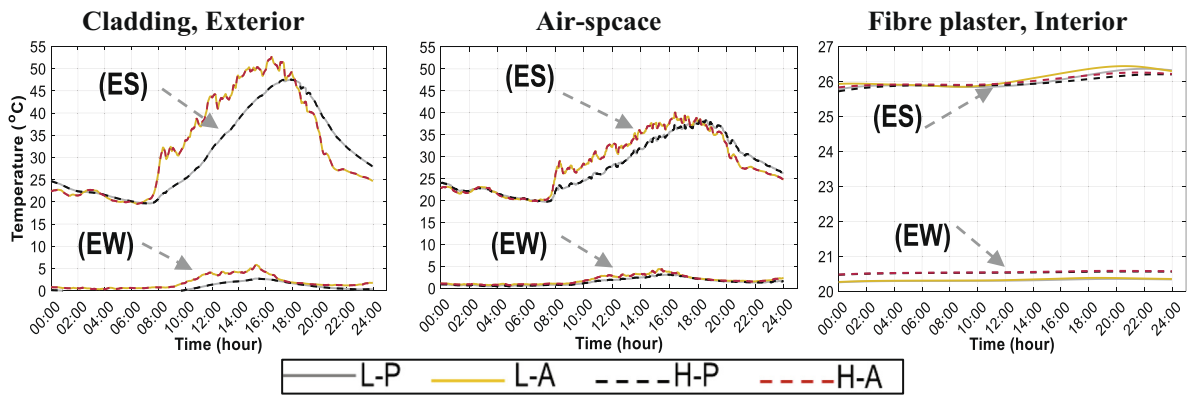

Fig. 17. Temperature profiles at the middle point on different surfaces in the wall structure with 45 mm cavity during extreme outdoor conditions (refer to Table 2 for abbreviations). Summer cases (ES) are upper curves, and winter cases (EW) are lower curves.

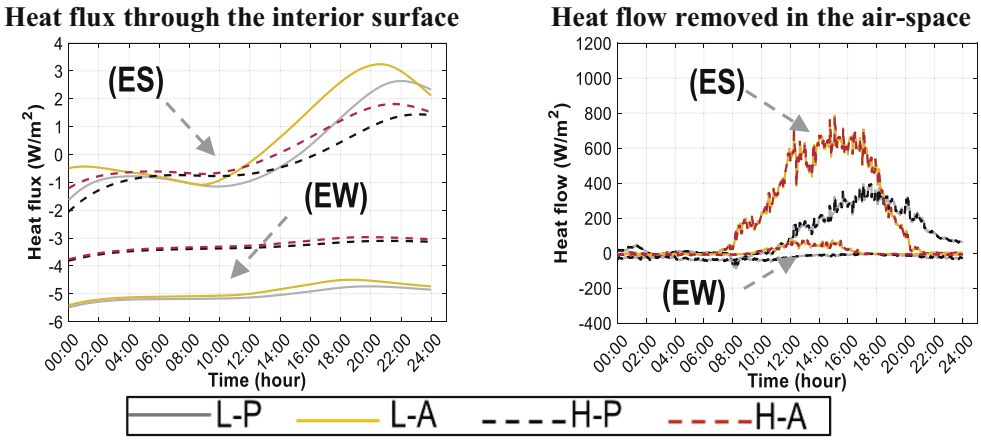

Fig. 18. Profiles of the heat flux through the interior surface and heat flow removed in the 45 mm air-space at the middle point in the wall during extreme outdoor conditions (refer to Table 2 for abbreviations). Summer cases (ES) are upper curves, and winter cases (EW) are lower curves.

has also been increased for 4 h in the wall structure with both passive and active facades.

4.6.3. Heat flow passing through the cavity

The amount of heat flow through the air-space is presented in Fig. 18. The maximum heat removed from the cavity in the passive and active facades in the hottest summer day are respectively 394.4 W/m^2 and 786.5 W/m^2. The values are lower compared to the results in the typical day. This could be attributed to the lower temperature gradient between the top and bottom of the air gap and also lower wind speed that acts as the driving force for the airflow on the hottest day compared to the typical day. Similar results can be observed for the winter case.

4.6.4. Electrical efficiency of the PV panel

The evaluation of the electrical efficiency during the hottest summer day is shown in Fig. 19. Due to the higher temperature of the interior surface of the PV panel in this scenario, the efficiency drops to 10.6% that is 0.4% lower compared to the typical day.

4.6.5. Transient responses of the wall assembly

The bar charts in Fig. 20 show the transient responses of the building envelope during extreme conditions. Compared to the typical days, it can be observed that the time lag of the *LP* case is decreased, while the values are increased in the *HP* case. In the case of the wall assembly with an active façade, however, the time lag is reduced in both lightweight and heavyweight wall cores. In contrast to the typical days, replacing the passive cladding with the active façade reduces the time lag of the wall assembly in both summer and winter conditions. The change in the outdoor condition in extreme days compared to the typical days has resulted in a different temperature distribution within the wall assembly, which consequently has changed the transient responses of the wall structure. By changing the lightweight wall core to a heavyweight structure, the time lag of the passive cladding increases for 1.15 h and 1.90 h, respectively, in summer and winter. The corresponding values for the active façade are 1.55 h and 1.08 h. The lowest time lag corresponds to the *LA-EW45*, and the highest value happens for the *HP-EW45*. Regarding the decrement factors shown in Fig. 20, it can be seen that the maximum values in summer and winter are respectively 0.021 and 0.030. The values are higher compared to the typical days. The maximum decrement factor corresponds to the *LP-EW45*, and the minimum value happens for the *HP-ES45*.

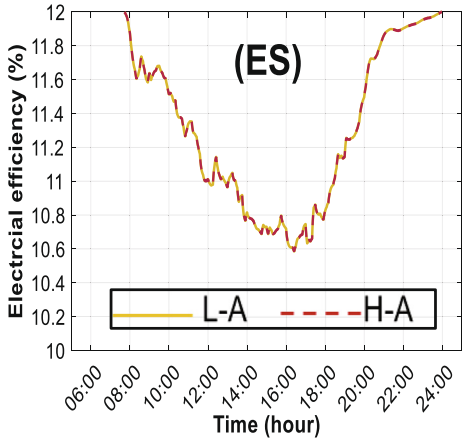

Fig. 19. Profiles of the electrical efficiency of the PV panel with 45 mm cavity during extreme outdoor conditions (only the period of the exposure to the solar radiation is shown, refer to Table 2 for abbreviations).

5. Discussion

In this section, a summary of the results is provided to outline the most important aspects of the present study. The impact of change in the wall structure and outdoor conditions on the temperature distribution, heat flux through the interior surface, heat flow leaving the air gap, the electrical efficiency of the PV module, and the time lag associated with the wall assembly are summarized in Table 6. Based on the results, replacing the passive cladding with an active façade has a considerable effect on the heat flow through the cavity and the time lag of the wall structure. The temperature distribution in the entire wall assembly, heat flux through the interior surface, and the electrical efficiency of the PV panel are more affected when extreme outdoor conditions than typical conditions are considered.

To further analyze the wall structures incorporating modern PV façades, which are attracting more attention in recent years, conditional density plots for selected variables are presented in Fig. 21, considering important performance criteria for designing active wall assemblies. The plots are classified according to the seasons, effective input categorical variables (thermal mass of the wall, thickness of the cavity, and reflective insulation presence on the cavity surface adjacent to the wall core), and output continuous parameters defining the performance of the wall (heat flux through

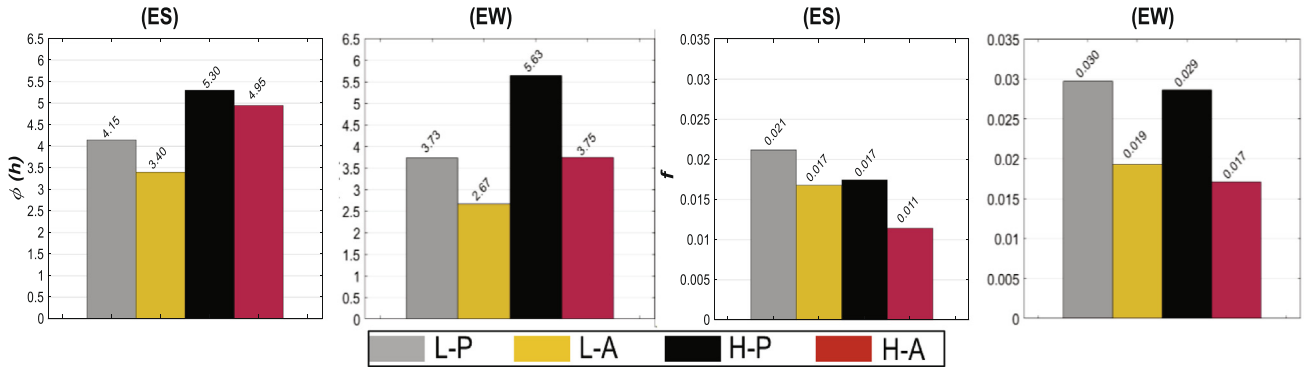

Fig. 20. Time lag and Deceremnt factor of the wall structure with 45 mm cavity during extreme outdoor conditions (refer to Table 2 for abbreviations).

Table 6
Overview of the results.

Change in the wall structure or outdoor condition	Effect on the results				
	Temperature	Heat flux through the interior surface	Heat flow in the cavity	Electrical efficiency	Time lag of the wall assembly
Replacing passive cladding with the active facade	Increases the cladding surface up to 18 °C (S), and up to 3 °C (W) Increases the airflow up to 5 °C (S), and up to 2 °C (W) Shifts the amplitude of the interior surface up to 2 h	Increases up to 2 times Shifts amplitude up to 2 h (S), and negligible effect (W)	Increases up to 4 times (S) and up to 2 times (W)	——	Increases up to 2 h (S), decreases up to 1 h (W) Higher with the lightweight wall structure compared to the heavyweight passive wall
Altering wall core from lightweight to heavyweight	Shifts the amplitude of the interior surface up to 2 h Negligible effect on other surfaces	Increases up to 1.5 times May increase or decrease depending on outdoor temperature (S), shifts amplitude up to 1 h (W)	No considerable effect	Negligible effect	Increases up to 1 h (S & W)
Enlarging cavity thickness	Decreases the surface and airflow up to 2.5 °C (S), and up to 1.5 °C (W)	Slightly increases (S), negligible effect (W)	Increases up to 1.5 times (S) and up to 1.2 times (W)	Slightly increases	No considerable effect
Using reflective insulation on the cavity surface adjacent to the wall core	Increases the cladding surface up to 3 °C, decreases the airflow up to 1 °C, insulation up to 4 °C, interior surface up to 0.2 °C	Increases up to 1.5 times (S), and negligible effect (W)	No considerable effect	Slightly decreases	Decreases up to 0.1 h (S), increases up to 0.12 h (W)
Changing the outdoor condition to extreme days	Increases the cladding surface up to 12 °C (S), decreases up to 13 °C (W), airflow up to 10 °C (S & W), increases the interior surface up to 0.4 °C	Switches the direction (S) with an increment up to 7 times (S), and up to 1.5 times (W)	Decreases up to 1.1 times (S) and up to 2 times (W)	Decreases up to 0.4%	Increases up to 1.3 h for passive façade (S), decreases up to 1 h for active façade (S), decreases up to 0.7 h for passive and active façades (W)

Note: The results are extracted from the plots presented in section 4 considering general trends, therefore, a few contradictory values with the results provided in the table might be seen at specific time durations throughout a day.

the interior space, heat flow in the cavity, and the electrical efficiency of the PV module). The plots in Fig. 21 show how the conditional distribution of each performance value dynamically changes over different categorical variables (only the results of scenarios simulated for typical days are examined for a proper generalization of the results).

Considering **the heat flux through the interior surface** as the first performance criteria, which should be minimized, the plots in Fig. 21-a1 reveal that the lightweight wall core can minimize the heat flux entering the indoor space in summer (or maximize the negative values shown on the plots of the heat flux, since negative values show the heat flow leaving indoors). As described in section 4.2, the higher indoor temperature compared to the outdoor temperature in summer has resulted in a higher heat flow leaving the indoor space using a lightweight wall core. In winter, however, the heavyweight wall core minimizes the heat flow leaving the indoor space as it has a higher probability once the heat flux values become closer to zero (Fig. 21-d1). The results show that the probability of minimizing heat flow through the interior space in summer is almost similar for both cavity thicknesses (Fig. 21-b1), while the air gap with 45 mm thickness has a slightly higher probability of minimizing heat flow, leaving the indoor space in winter (Fig. 21-e1). Moreover, the absence of reflective insulation has a slightly better effect on minimizing heat flux through the interior space in summer (i.e., a maximum negative value in Fig. 21-c1), while a similar probability is obtained with the case of absence of reflective insulation in winter (i.e., a minimum negative value in winter in Fig. 21-f1).

The **heat flow leaving the cavity** is considered as the next performance parameter, which should be maximized to boost the potential of cooling the PV façade. Based on the results shown, the heavyweight wall core has a slightly higher probability of maximizing the heat flow in the air gap both in summer and winter (Fig. 21-a2,d2). The results show that the larger air-space is more effective in yielding higher heat flow leaving the cavity in summer and winter (Fig. 21-b2,e2). Regarding the effect of the presence of reflective insulation, the plots reveal that the probability is almost similarly distributed for both surfaces with low and high emissivity in both seasons (Fig. 21-c2,e2).

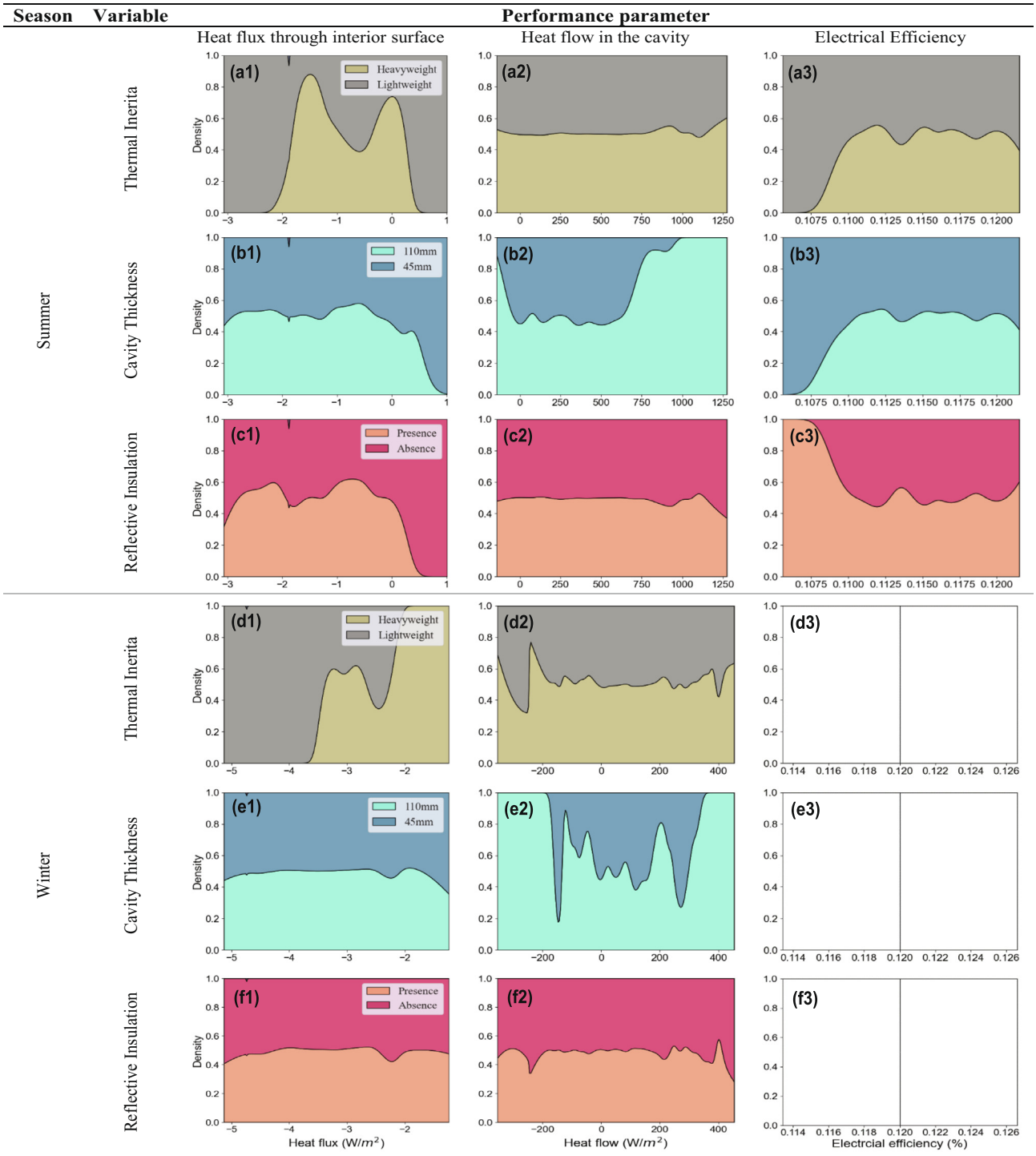

891 Figure 21: Conditional density plots of the results

Fig. 21. Conditional density plots of the results.

The plots in Fig. 21 (a3, b3, c3) show that the thermal mass of the wall, thickness of the air gap, and the presence of reflective insulation have not a considerable effect on maximizing **the electrical efficiency** of the PV panel in summer. As described in section 4.5, the single lines shown in the conditional density plots under electrical efficiency in winter (Fig. 21-d3, e3, f3) depict the highest efficiency obtained for all cases due to having the temperature of the PV panel always lower than the reference temperature.

It should be highlighted that **the time lag** associated with the wall core could be considered as another performance parameter. However, this parameter is not continuous, and the corresponding values are presented in Fig. 16. According to the results, the wall assembly with heavyweight wall core has the greatest time lag, while the thickness of the cavity and the presence of reflective insulation have a negligible effect on maximizing the transient responses of the building envelope with the BIPV façade.

6. Conclusion

The thermal mass of the materials used in a building envelope, the type of the façade, the thermo-physical properties of a naturally ventilated air-space behind external claddings, and the dynamic variation of the outdoor conditions are among the most important factors that contribute to the performance of wall structures. In the present study, the lightweight and heavyweight wall cores separated from passive (fiber cement) or active (BIPV) facades by incorporating a ventilated cavity were investigated using a 2-D computational model validated against experimental measurements. The thermal performance and electrical efficiency of various wall assemblies were analyzed during typical and extreme days in summer and winter of 2019 in Lausanne (Switzerland).

The results confirm the complexity of the problem due to the interaction of several parameters. Based on the results, it was revealed that:

- Changing the wall core from a lightweight to a heavyweight can increase the heat flux through the interior surface up to 1.5 times and shifts its amplitude up to 1 h in winter, but may increase or decrease the heat flow in summer depending on the outdoor conditions
- Replacing the passive cladding with an active facade interestingly results in higher time lag with the lightweight wall structure compared to the heavyweight passive wall assembly
- Enlarging the cavity thickness increases the heat flow passing through the cavity up to 50% in summer and winter
- Using reflective insulation on the cavity surface adjacent to the wall core increases the heat flux through the interior surface up to 1.5 times in summer, but has a negligible effect in winter
- When extreme days are considered, the time lag associated with the wall structure increases for the passive cladding compared to BIPV façade in summer, which is in contrast to the results observed during typical days

This study was carried out to highlight the fact that switching towards modern facades could significantly vary the thermal performance of the building envelope. The change might be favorable or not, depending on the indoor and outdoor conditions, materials used in the rest of the wall structure, and the absence or presence of the ventilated air-space within the assembly. The simulations in this study were performed assuming a 2-dimensional geometry. However, the 3-dimensional effects, including the variation of the temperature distribution through the width of the surfaces, need to be evaluated in the future, employing CFD simulations or using measurements from in-field studies. The presence of narrow passages between the PV modules in the case of studying high-rise buildings could affect the airflow pattern in the cavity and requires particular attention in future works. The results provided in this study could be generalized for other types of PV panels that have direct dependence of efficiency from temperature, although the electrical efficiency of PV modules based on various technologies is expected to be different. The aforementioned outcomes could be applied for passive claddings with relatively low thermal mass. Therefore, additional analysis is needed for the claddings with high inertia, such as a brick wall.

Declaration of competing interest

The authors declare that they have no known competing financial interests or personal relationships that could have appeared to influence the work reported in this paper.

References

[1] Aelenei, L. E. (2006). Thermal Performance of a Naturally Ventilated Cavity Wall.
[2] C. Afonso, A. Oliveira, Solar chimneys: Simulation and experiment, Energy Build. 32 (1) (2000) 71–79.
[3] R.A. Agathokleous, S.A. Kalogirou, Part I: Thermal analysis of naturally ventilated BIPV system: Experimental investigation and convective heat transfer coefficients estimation, Sol. Energy 169 (2018) 673–681.
[4] R.A. Agathokleous, S.A. Kalogirou, Part II: Thermal analysis of naturally ventilated BIPV system: Modeling and Simulation, Sol. Energy 169 (2018) 682–691.
[5] M. Ahmed-Dahmane, A. Malek, T. Zitoun, Design and analysis of a BIPV/T system with two applications controlled by an air handling unit, Energy Convers. Manage. 175 (2018) 49–66.
[6] S.A. Al-Sanea, M.F. Zedan, S.N. Al-Hussain, Effect of thermal mass on performance of insulated building walls and the concept of energy savings potential, Appl. Energy 89 (1) (2012) 430–442.
[7] H. Asan, Effects of wall's insulation thickness and position on time lag and decrement factor, Energy Build. 28 (3) (1998) 299–305.
[8] H. Asan, Numerical computation of time lags and decrement factors for different building materials, Build. Environ. 41 (5) (2006) 615–620.
[9] Ashrae, Handbook—Fundamentals, SI edition., American Society of Heating, Refrigerating and Air Conditioning Engineers Inc., Atlanta, Georgia, 2021.
[10] N. Aste, A. Angelotti, M. Buzzetti, The influence of the external walls thermal inertia on the energy performance of well insulated buildings, Energy Build. 41 (11) (2009) 1181–1187.
[11] M. Bagarić, I. Banjad Pečur, B. Milovanović, Hygrothermal performance of ventilated prefabricated sandwich wall panel from recycled construction and demolition waste – A case study, Energy Build. 206 (2020) 109573, https://doi.org/10.1016/j.enbuild.2019.109573.
[12] A. Bejan, Heat Transfer, Wiley, New York, 1993.
[13] A. Brambilla, T. Jusselme, Preventing overheating in offices through thermal inertial properties of compressed earth bricks: A study on a real scale prototype, Energy Build. 156 (2017) 281–292.
[14] C. Buratti, D. Palladino, E. Moretti, R. Di Palma, Development and optimization of a new ventilated brick wall : CFD analysis and experimental validation, Energy Build. 168 (2018) 284–297.
[15] Chiu, M. S., Hou, S. P., Tzeng, C. T., & Lai, C. M. (2015). Experimental Investigations on the Thermal Performance of the Ventilated BIPV Wall, *15*(3), 613–618.
[16] W. Cho, S. Iwamoto, S. Kato, Condensation risk due to variations in airtightness and thermal insulation of an office building in warm and wet climate, Energies 9 (11) (2016) 875, https://doi.org/10.3390/en9110875.
[17] S.W. Churchill, H.H.S. Chu, Correlating equations for laminar and turbulent free convection from a vertical plate, Int. J. Heat Mass Transf. 18 (11) (1975) 1323–1329.
[18] H. Dehra, An investigation on energy performance assessment of a photovoltaic solar wall under buoyancy-induced and fan-assisted ventilation system, Appl. Energy 191 (2017) 55–74.
[19] R.F. De Masi, S. Ruggiero, G.P. Vanoli, Hygro-thermal performance of an opaque ventilated façade with recycled materials during wintertime, Energy Build. 245 (2021) 110994.
[20] S. Fantucci, V. Serra, C. Carbonaro, An experimental sensitivity analysis on the summer thermal performance of an Opaque Ventilated Façade, Energy Build. 225 (2020) 110354, https://doi.org/10.1016/j.enbuild.2020.110354.
[21] G.K. Filonenko, Formula dlya koeffitsienta gidravlicheskogo soprotivleniya gladkikh trub (Formula for the Coefficient of Fluid Resistance of Smooth Pipes). - Izvestiya VTI, No. 10 (162) (1948).
[22] G. Finch, The Performance of Rainscreen Walls in Coastal British Columbia, University of Waterloo, 2007.
[23] A. Gagliano, S. Aneli, Analysis of the energy performance of an Opaque Ventilated Façade under winter and summer weather conditions, Sol. Energy 205 (2020) 531–544.
[24] G. Gan, Effect of air gap on the performance of building-integrated photovoltaics, Energy 34 (7) (2009) 913–921.
[25] H. Ge, Y. Ye, Investigation of Ventilation Drying of Rainscreen Walls in the Coastal Climate of British Columbia, Thermal Performance of Exterior Envelopes of Whole Buildings X International Conference, 2007.
[26] G.M. Girma, F. Tariku, Experimental investigation of cavity air gap depth for enhanced thermal performance of ventilated rain-screen walls, Build. Environ. 194 (2021) 107710, https://doi.org/10.1016/j.buildenv.2021.107710.
[27] F. Guignard, D. Mauree, M. Lovallo, M. Kanevski, L. Telesca, Fisher-Shannon complexity analysis of high-frequency urban wind speed time series, Entropy 21 (1) (2019) 1–11.
[28] I. Guillén, V. Gómez-Lozano, J.M. Fran, P.A. López-Jiménez, Thermal behavior analysis of different multilayer façade: Numerical model versus experimental prototype, Energy Build. 79 (2014) 184–190.
[29] G. Hailu, P. Dash, A.S. Fung, Performance evaluation of an air source heat pump coupled with a building-integrated photovoltaic/thermal (BIPV/T) System under cold climatic conditions, Energy Procedia 78 (2015) 1913–1918.
[30] C.E. Hagentoft, Introduction to Building Physics, Studentlitteratur, Lund, 2001.
[31] D. Heim, A. Wieprzkowicz, Attenuation of temperature fluctuations on an external surface of thewall by a phase change material-activated layer, Applied Sciences 8 (1) (2018) 11.

[32] J. Holman, Heat transfer, 2nd edition., McGraw-Hill, New York, 1968.
[33] ISO Standard 6946, (2017). Building components and building elements — Thermal resistance and thermal transmittance — Calculation methods, Geneva.
[34] F.P. Incropera, Fundamentals of Heat and Mass Transfer (6th edition), John Wiley & Sons, 2007.
[35] Integrated Environmental Solutions. Reference Data. Accessed on 13th August 2021. https://www.iesve.com.
[36] Kotaro Kawajiri, Takashi Oozeki, Yutaka Genchi, Effect of temperature on PV potential in the world, Environ. Sci. Technol. 45 (20) (2011) 9030–9035.
[37] Köppen, Wladimir (1884). Translated by Volken, E.; Brönnimann, S. "Die Wärmezonen der Erde, nach der Dauer der heissen, gemässigten und kalten Zeit und nach der Wirkung der Wärme auf die organische Welt betrachtet" [The thermal zones of the earth according to the duration of hot, moderate and cold periods and to the impact of heat on the organic world)]. Meteorologische Zeitschrift (published 2011). 20 (3): 351–360.
[38] A. Kylili, P.A. Fokaides, Investigation of building integrated photovoltaics potential in achieving the zero energy building target, Indoor Built Environ. 23 (1) (2014) 92–106.
[39] J. Langmans, S. Roels, Experimental analysis of cavity ventilation behind rainscreen cladding systems: A comparison of four measuring techniques, Build. Environ. 87 (2015) 177–192.
[40] S.-K. Lau, Y. Zhao, V. Shabunko, Y. Chao, S.S.-Y. Lau, A. Tablada, T. Reindl, Optimization and evaluation of naturally ventilated BIPV façade design, Energy Procedia 150 (2018) 87–93.
[41] L. Long, H. Ye, The roles of thermal insulation and heat storage in the energy performance of the wall materials: a simulation study, Nat. Publ. Group (2016) 1–9.
[42] V. Manuel, S. Francés, E. José, S. Escriva, J. Manuel, P. Ojer, G. Silva, Modeling of ventilated facades for energy building simulation software, Energy Build. 65 (2013) 419–428.
[43] C. Marinosci, P.A. Strachan, G. Semprini, G.L. Morini, Empirical validation and modelling of a naturally ventilated rainscreen facade building, Energy Build. 43 (4) (2011) 853–863.
[44] Mauree, D., Deschamps, L., Becquelin, P., Loesch, P., & Scartezzini, J. L. (2017). Measurement of the impact of buildings on meteorological variables. *Building Simulation Applications, BSA 2017,* 3rd IBPSA conference, Bozen-Bolzano, Italy.
[45] L. Mei, D. Infield, U. Eicker, V. Fux, Thermal modelling of a building with an integrated ventilated PV façade, Energy Build. 35 (6) (2003) 605–617.
[46] B. Meyer, M. Spinu, T. Weston, H. Kuhlman, Impact of low-E WRB facing an air cavity on the R-value of a wall system, ASHRAE 11 (2019) 63–67.
[47] E. Meyer, S. Ziuku, M. Simon, O. Overen, Building integrated photovoltaics with passive solar heating and cooling, 31st Eur. Solar Energy Conf. Exhibit. 6 (11) (2015) 2642–2645.
[48] R. Na, Z. Shen, Assessing cooling energy reduction potentials by retrofitting traditional cavity walls into passively ventilated cavity walls, Build. Simul. (2020) 1–15.
[49] Nusselt, W., and Jürges, W. (1922). Die Kühlung einer ebenen Wand durch einen Luftstrom (The cooling of a plane wall by an air flow), Gesundheits Ingenieur 52. Heft, 45. Jahrgang, 641–642.
[50] Nemry, F., & Uihlein, A. (2008). *Environmental Improvement Potentials of Residential Buildings (IMPRO-Building).*
[51] B. Nghana, F. Tariku, G. Bitsuamlak, Assessing ventilation cavity design impact on the energy performance of rainscreen wall assemblies: A CFD study, Build. Environ. 107789 (2021).
[52] M.I. Nizovtsev, V.N. Letushko, V.Y. Borodulin, A.N. Sterlyagov, Experimental studies of the thermo and humidity state of a new building facade insulation system based on panels with ventilated channels, Energy Build. 206 (2020) 109607.
[53] S. Pantic, L. Candanedo, A.K. Athienitis, Modeling of energy performance of a house with three configurations of building-integrated photovoltaic/thermal systems, Energy Build. 42 (10) (2010) 1779–1789.
[54] M. Rahiminejad, D. Khovalyg, Impact of the Ventilated Cavity on the Thermal Performance of Traditional Wall Structures, ASHRAE Transactions 127 (2021) 187–195.
[55] M. Rahiminejad, D. Khovalyg, Review on ventilation rates in the ventilated air-spaces behind common wall assemblies with external cladding, Build. Environ. 190 (2021) 107538.
[56] M. Rahiminejad, D. Khovalyg, Thermal resistance of ventilated air-spaces behind external claddings; definitions and challenges (ASHRAE 1759-RP), Sci. Technol. Built Environ. 27 (6) (2021) 788–805.
[57] M. Rahiminejad, D. Khovalyg, Thermal resistance of the ventilated air-spaces behind external claddings; theoretical definition and a parametric study, 2069, Journal of Physics: Conference Series, 2021.
[58] M. Rahiminejad, D. Khovalyg, Measuring the effective thermal resistance of ventilated air-spaces behind common wall assemblies: theoretical uncertainty analysis and recommendations for the hot box method modifications, Sci. Technol. Built Environ., 2021, In press.
[59] P.K.S. Rathore, S.K. Shukla, N.K. Gupta, Yearly analysis of peak temperature, thermal amplitude, time lag and decrement factor of a building envelope in tropical climate, J. Build. Eng. 31 (2020) 101459.
[60] P. Sánchez-Palencia, N. Martín-Chivelet, F. Chenlo, Modeling temperature and thermal transmittance of building integrated photovoltaic modules, Sol. Energy 184 (2019) 153–161.
[61] Í.P. Dos Santos, R. Rüther, The potential of building-integrated (BIPV) and building-applied photovoltaics (BAPV) in single-family, urban residences at low latitudes in Brazil, Energy Build. 50 (2012) 290–297.
[62] P. Seferis, P. Strachan, A. Dimoudi, A. Androutsopoulos, Investigation of the performance of a ventilated wall, Energy Build. 43 (9) (2011) 2167–2178.
[63] S. Schwab, J. Rime, G. Jaquerod, L. Rinquet, G. Rey, R. Camponovo, et al., Rénovation énergétique: approche globale pour l'enveloppe du bâtiment: études de densification, HEPIA - Genève. (2018), 978-2-9701005-2-2.
[64] SIA, Standardized data for building energy modeling (SIA 2024:2015), Zurich, Switzerland, 2015.
[65] M.E.A. Slimani, M. Amirat, I. Kurucz, S. Bahria, A. Hamidat, W.B. Chaouch, A detailed thermal-electrical model of three photovoltaic/thermal (PV/T) hybrid air collectors and photovoltaic (PV) module: Comparative study under Algiers climatic conditions, Energy Convers. Manage. 133 (2017) 458–476.
[66] F. Stazi, G. Ulpiani, M. Pergolini, C. Di Perna, M. D'Orazio, The role of wall layers properties on the thermal performance of ventilated facades: Experimental investigation on narrow-cavity design, Energy Build. 209 (2020).
[67] S.S. Stevens, On the Theory of Scales of Measurement, Science 103 (2684) (1946) 677–680.
[68] Straube, J., & Finch, G. (2009). Report 0906: Ventilated wall claddings: review, field performance, and hygrothermal modeling. *Building science corporation.*
[69] W.C. Swinbank, Long-wave radiation from clear skies, Q. J. R. Meteorolog. Soc. 89 (381) (1963) 339–348.
[70] Swisspor AG. Accessed on 13th August 2021. Mur extérieur-Mur hors sol-Façade ventilée isolée. Récupéré sur Swisspor: https://www.swisspor.ch/.
[71] F. Tariku, E. Iffa, Empirical model for cavity ventilation and hygrothermal performance assessment of wood frame wall systems: Experimental study, Build. Environ. 157 (2019) 112–126.
[72] Thermtest Instruments. Accessed on 13th August 2021. https://thermtest.com/.
[73] K. Ulgen, Experimental and theoretical investigation of effects of wall's thermophysical properties on time lag and decrement factor, Energy Build. 34 (3) (2002) 273–278.
[74] M. Van Belleghem, M. Steeman, A. Janssens, M. De Paepe, Heat, air and moisture transport modelling in ventilated cavity walls, J. Build. Phys. 38 (4) (2015) 317–349.
[75] N. Vargaftik, Handbook of Physical Properties of Liquids and Gases Pure Substances and Mixture, Springer-Verlag, Berlin Heidelberg, Berlin, 1975.
[76] Y. Wang, W. Tian, J. Ren, L. Zhu, Q. Wang, Influence of a building's integrated-photovoltaics on heating and cooling loads, Appl. Energy 83 (9) (2006) 989–1003.
[77] O. Zogou, H. Stapountzis, Flow and heat transfer inside a PV/T collector for building application, Appl. Energy 91 (1) (2012) 103–115.
[78] Zürcher C, F. T. (2018). Bauphysik: Bau & Energie. Zürich: vdf.